2016

Millimeter – Wave/Terahertz Chirped Michelson Interferometer Techniques for Sub Surface Sensing

Dinesh Amal Mirando
Wright State University

MILLIMETER – WAVE/TERAHERTZ CHIRPED MICHELSON INTERFEROMETER TECHNIQUES FOR SUB SURFACE SENSING

A thesis submitted in partial

fulfillment of the requirements for

the degree of Master of Science

By

Dinesh Amal Mirando

2016

Wright State University

WRIGHT STATE UNIVERSITY

GRADUATE SCHOOL

January 09, 2017

I HEREBY RECOMMEND THAT THE THESIS PREPARED UNDER MY SUPERVISION BY Dinesh Amal Mirando ENTITLED Millimeter-wave/terahertz chirped Michelson interferometer techniques for sub surface sensing BE ACCEPTED IN PARTIAL FULFILLMENT OF THE REQUIREMENTS FOR THE DEGREE OF Master of Science.

_____
Douglas T. Petkie, Ph.D.
Thesis Director

_____
Jason Deibel, Ph.D.
Chair, Department of Physics

Committee on
Final Examination

_____
Douglas T. Petkie, Ph.D.

_____
Jason Deibel, PhD

_____
Jerry Clark, Ph.D.

_____
Robert E. W. Fyffe, Ph.D.
Vice President for Research and
Dean of the Graduate School

Abstract

Mirando, Dinesh Amal M.S. Department of Physics, Wright State University 2016. Millimeter-wave/terahertz chirped Michelson interferometer techniques for sub surface sensing.

Over the last couple of decades, the field of millimeter-wave (mmW) and terahertz (THz) radiation has seen an accelerated growth thanks to developments in high quality mmW/THz sensors. These developments have contributed to many useful applications in the fields of medicine, security, construction, etc. Non-destructive evaluations such as the detection of defects in materials is currently one of the major applications of mmW/THz radiation. These evaluations are performed using mmW/THz continuous-wave radar systems. In this study, we discuss how Frequency Modulated Continuous Wave (FMCW) techniques can enhance sensing applications through the use of a Michelson interferometer. This allows multiple objects or surfaces to be range resolved. Range resolution is dependent upon the bandwidth of the frequency sweep of the FMCW system and we will discuss several experiments performed that lead to achieving a range resolution of around 1mm.

Acknowledgements

I wish to thank my advisor Dr Doug Petkie for the wholehearted support and guidance given from the beginning till the completion of my research. I would also like to thank my committee members Dr Jason Deibel and Dr Jerry Clark for their time and valuable feedback on my thesis material.

I wish to extend my gratitude to former graduate student, Robert Schueler for sharing his knowledge and expertise in this field. I also would like to thank undergraduate students Matthew Larson for programming several instruments that were part of my study and Michael Higgins for his support in setting up and conducting several experiments.

Finally, I would like to thank my lovely wife, Remona Heenkenda for all the support, encouragements and understanding which made all of this possible.

TABLE OF CONTENTS

LIST OF FIGURES

LIST OF TABLES

Chapter 1

Introduction

Millimeter-wave/Terahertz radiation is defined as the region of the electromagnetic spectrum which lies between microwave and infrared radiation. It contains a band of frequencies from 30 GHz to 3 THz with wavelengths between 1 cm to 100 μm. Millimeter-wave/Terahertz is probably the least utilized form of radiation in the electromagnetic spectrum due to lack of inexpensive and mature technologies. Millimeter-wave (mmW) / terahertz (THz) radiation is non-ionizing and its ability to penetrate through a variety of non-conducting materials has paved a way to significant developments in the last decade or so. Today, mmW/THz technology is being used in a wide variety of useful applications in medical sciences, homeland security, construction, automotive, aviation etc.

Terahertz technology is one of the frontrunners in defense and homeland security. From airport body scanners to concealed weapons detection, the technology is making rapid progress thanks to developments in high quality mmW/THz sensors. Also, the mmW/THz research community across the globe is growing, leading to more collaborative research and knowledge exchange with major scientific journals dedicating separate chapters for THz sciences which validates this claim. The IEEE Transactions on Terahertz Science and Technology is one such leading scientific journal that covers

terahertz science, technology, instruments, and applications. Another being the Journal of Infrared, Millimeter, and Terahertz Waves.

1.1 NDE using mmW/Terahertz

Non-destructive evaluation (NDE) is a method for evaluating the structure and composition of a material without altering its properties. mmW/THz based sensing systems have been developed to inspect and characterize various materials that are otherwise inaccessible using other evaluation methods. These systems are capable of spatially resolving targets or hidden defects within visibly opaque dielectric materials. Furthermore, mature microwave technologies and established optical techniques can be combined to develop a variety of mmW/THz sensing systems for a number of applications.

Concealed weapons detection is one of the major applications of mmW/THz based sensing systems and Cooper et al. [1] have demonstrated a fast, high resolution THz imaging system in the ~600-700 GHz range. This ultra-wide bandwidth terahertz imaging radar system was capable of performing person-borne concealed object detection at a standoff distance of 25 m. Another system developed for concealed weapons detection by Sheen et al. [2] utilizing ~350 GHz, active, wideband, 3D radar imaging system, successfully operated at ranges up to 10+ meters and was capable of performing fast scanning (10-20 seconds) of individuals for concealed weapons detection. Furthermore, Heimbeck *et al.* [3] constructed an off-axis Fresnel interferometric imager using a highly coherent, narrow band CW source in the 0.3 – 1.0 THz frequency region to acquire

holograms that achieved sub-millimeter transverse spatial resolution of ~2 μm through amplitude and phase reconstructed images.

1.2 Target detection using mmW/THz

mmW/THz has numerous advantages over traditional RADAR systems in range determination. The main advantage is in range (depth or longitudinal) resolution, where mmW/THz systems can achieve accuracies on the order of the millimeters. These mmW/THz systems are also capable of velocity measurements of moving targets and have been successful in remotely sensing vital signs such as respiration and heart rates of individuals over standoff distances of up to 10 m [4]. These systems were developed utilizing a frequency shift keying continuous wave (CW) Michelson Interferometer and CW heterodyne systems that performed phase change measurements associated with the cardiopulmonary activities (heart beat and respiration) of the individuals [5-7]. The techniques of these previous studies could not discern multiple surfaces/targets at different ranges (distances) within the beam and could only monitor the motion of one surface/target at a time. The study presented in this thesis was primarily focused on identifying multiple stationary targets at different ranges within the same beam and the main detection technique used was the frequency modulated continuous wave (FMCW) radar.

1.3 The FMCW RADAR

Frequency modulated Continuous wave (FMCW) Radar is a short range radar system capable of determining distances. Conventional CW radars do not have the capability of measuring the time delay between the emitted and received signal, which makes it impossible to locate the object. The importance of frequency modulation is that it enables the system to measure this time delay by measuring the shifted frequency of the return signal, thus making range determination possible. Also, traditional pulsed radar systems are not capable of determining short ranges (~1 cm) as they require very short pulses typically around 33 picosecond. Electronic radar systems are typically limited to pulses greater than 1 nanosecond, which makes short range measurements at 1 mm impossible.

FMCW techniques have been successfully used in the development of mmW/THz based sensing systems and Cooper *et al.* [8] have demonstrated a high resolution 3D imaging radar system in the 576-605 GHz range capable of detecting weapons concealed by clothing at standoff ranges of 4–25 m. This coherent radar system utilized standard FMCW radar techniques coupled with optical systems to achieve a 1cm scale resolution in all three dimensions. Quast *et al.* [9] investigated the use of an all-electronics FMCW based mmW/THz imaging system for the non-destructive testing of foam materials and glass fiber composite (GFC) samples. The GFC structures were evaluated in the 65- 110 GHz range, leading to a penetration depth of about 2 cm and a spatial (transverse) resolution of about 3 mm while the foam structure was measured in the 230 - 320 GHz range, leading to a spatial resolution of 1 mm.

1.4 FMCW interferometry using a Michelson interferometer

In this study, FMCW techniques are developed using a Michelson interferometer to resolve objects at different depths that would lead to range determination. This technique would ultimately lead to the development of a 3D imaging system that would perform depth resolved subsurface sensing. An alternate method would be to use THz-time domain systems (TDS) that are capable of doing this naturally via time-resolved returns of ultra-fast pulses [10] (i.e. femto-second timing techniques). The study was based on using a system with all electronics as opposed to an ultrafast laser in the time domain systems. This all electronics system was coupled with wide band FMCW techniques to perform the equivalent of time domain systems.

Chapter 2

Background

2.1 Michelson interferometer

A Michelson interferometer produces an interference pattern by splitting a monochromatic light beam using a beam splitter. Each nearly equal intensity beam travels different distances, is reflected off of mirrors (or a mirror and a target), and then recombined to a resultant intensity. If the path lengths of the two waves are different, the light waves will be at different phases when they are recombined. The addition of these two waves will produce an interference pattern (fringes) that depends on the path difference.

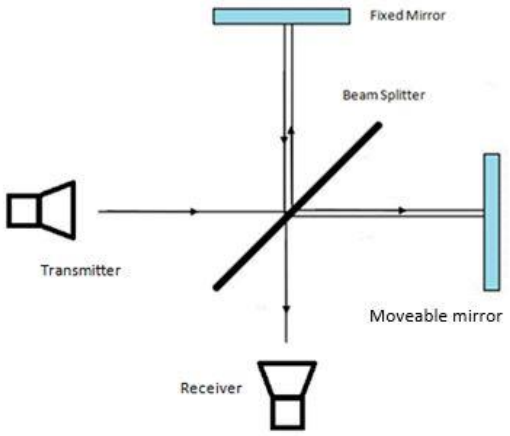

Figure 2.1: A basic Michelson interferometer with a fixed and a moveable mirror.

The Michelson interferometer has been a very useful instrument since it was invented in the late 1800s and has made significant contributions to some major discoveries over the last century. One recent major achievement is in detecting the gravitational waves [11]. The Laser Interferometer Gravitational-Wave Observatory (LIGO) is the instrument that helped scientists observe the presence of cosmic waves that was predicted by Albert Einstein in 1916 in his general theory of relativity.

LIGO's setup is basically a Michelson interferometer combined with a Fabry Perot interferometer. A Fabry Perot interferometer consists of an etalon (two reflecting mirrors) that produces multiple reflections. Michelson interferometer in LIGO is by far the largest ever built [12]. Each of its arms span 4 km and the system is about 360 times larger than the one used in the famous Michelson-Morley experiment. LIGOs ability to detect extremely small phase changes was the most crucial factor that made the discovery possible.

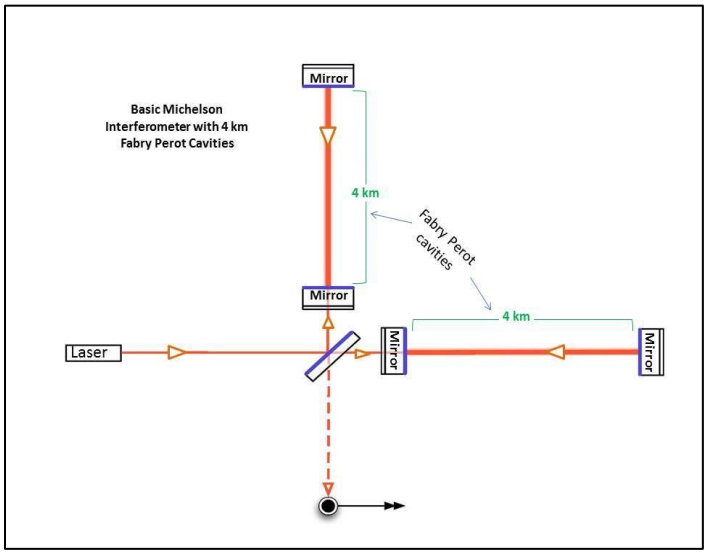

Figure 2.2: Main components of the LIGO instrument that consists of a Michelson interferometer and Fabry Perot cavities (*LIGO*, Caltech).

2.2 Michelson Interferometer basics

The electric field associated with a propagating wave can be expressed as

$$E(r,t) = E_0(r)e^{-j(kr-\omega t+\phi)} \qquad (2.1)$$

where E_0 is the wave amplitude , k is the propagation vector and r is the position vector, ω is the angular frequency, t is the time, and ϕ is an arbitrary phase constant. In a typical Michelson Interferometer, the superposition of linearly polarized monochromatic waves of the same frequency [13]. The actual frequency cannot be measured, therefore we measure the time averaged power so that the exponential term containing temporal information is averaged out to be a constant. Also, the detectors used do not have the bandwidth to measure the frequencies instantaneously. Under these circumstances, the temporal term is omitted and only the complex amplitude is taken into consideration. Therefore, the equation simplifies to

$$E(r) = E_0 e^{-j(kr+\phi)} \qquad (2.2)$$

The intensity of the propagating wave is defined as the average energy per unit area per unit time and is usually represented by the time average of the square of the electric field. So, for a linearly polarized monochromatic wave, the intensity can be represented by

$$I(r) \propto |E(r)|^2 \qquad (2.3)$$

For the Michelson interferometer, we can express the intensity of the resultant electric field due to interference of two linearly polarized, monochromatic plane waves by

$$I(r) \propto |E_1(r) + E_2(r)|^2 \qquad (2.4)$$

When simplified using complex conjugates, this equation becomes

$$I(r) = I_1 + I_2 + 2\sqrt{I_1 I_2}\cos[(k_1 r_1 - k_2 r_2) - (\phi_1 - \phi_2)] \quad (2.5)$$

where k_1, k_2 are propagation vectors of wave 1 and wave 2 respectively and ϕ_1 & ϕ_2 are their initial phases.

Since both waves are generated from the same source, $k_1 = k_2 = k$ and $r_1 - r_2 = l_1 - l_2$ .The above equation simplifies to

$$I(l_1, l_2) = I_0\{1 + V\cos(k(l_2 - l_1))\} \quad (2.6)$$

where l_1&l_2 are the optical path lengths of wave 1 and wave 2

I_0 is the average intensity of the electric field given by

$$I_0 = I_1 + I_2 \quad (2.7)$$

V is the visibility of the fringes given by

$$V = \frac{2\sqrt{I_1 I_2}}{I_1 + I_2} \quad (2.8)$$

The resulting intensity is governed by the optical path difference (OPD) between the two rays. So it can be rewritten in terms of frequency by

$$I(OPD) = I_0\left\{1 + Vcos\left[2\pi\left(\frac{OPD}{c}\right)\nu\right]\right\} \quad (2.9)$$

where the OPD for the Michelson interferometer is twice the difference in the arm lengths due to reflection.

The cosine term in this equation carries information related to the interference of the two waves, which depends on the path difference between them. This equation plays a vital role in experimentally determining the different between two surfaces. However, there is

a difference between a Michelson Interferometer and our FMCW system. In our experiments, the OPD will be a constant while we linearly sweep the frequency,ν over a bandwidth. This results in a 'frequency' (or number of interference fringes for a given sweep bandwidth) of the interference pattern that can be identified as $f = \frac{OPD}{c}$ and $\omega = 2\pi f$, thus giving

$$I(OPD) = I_0\{1 + V\cos[\omega\nu]\} \tag{2.10}$$

2.3 The FMCW RADAR

The model above is based on the Michelson Interferometer. An alternative and equivalent model is to consider the time delay between the two signals that arrive at the detector that is a result of the different path lengths. For an FMCW system, the transmitted is linearly swept through a range of frequencies, from f_0 to f_1 over the time T, as shown in Figure 2.3.

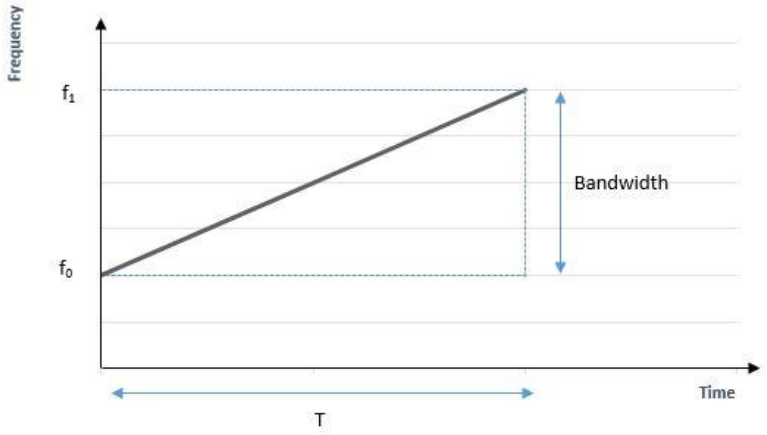

Figure 2.3: Frequency sweep in FMCW with a T(s) sweep and $(f_1 - f_0)$ bandwidth.

If we consider the difference between the two paths to be R, which would be (L_2-L_1) in the case of the Michelson Interferometer above, then the time delay, τ, between the two signals is given by

$$\tau = \frac{2R}{c} \qquad (2.11)$$

where c is the speed of light in the medium. Since the transmitter is being swept linearly in time, this time delay will result is a difference in frequency between the two reflected waves, as shown in Figure 2.4.

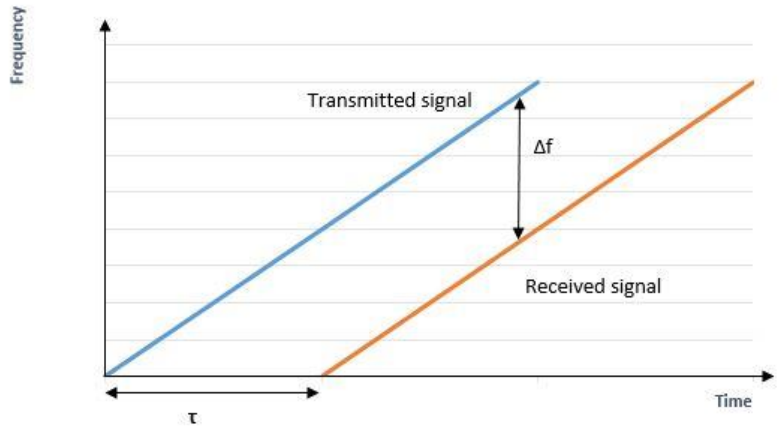

Figure 2.4: Frequency shift in the received signal with a time delay τ.

The mixing of the two signals at the detector produces a beat frequency which is proportional to distance to the object. The beat frequency is equivalent to the expression for f in Eq. (2.10) and also depends on the sweep rate, T.

There are many methods to modulate the signal and the most widely used method is to linearly increase the frequency. This method reduces the cost of design and also simplifies the signal processing. Sawtooth modulation is the most commonly used modulation type in FMCW radar while other modulation types include sine, square and triangular modulation. In this study, triangular modulation was used and when compared to the sawtooth modulation, there is a factor of two associated with the triangular modulation frequency related to the sweep rate *T*.

2.4 FMCW range resolution

The range resolution depends on the bandwidth of the sweep and is given by

$$\Delta R = \frac{C}{2B} \qquad (2.12)$$

where *B* is the bandwidth of the sweep, i.e. $f_1 - f_0$. A greater bandwidth in the frequency sweep allows for better range resolution.

Time delay measurements are performed using a Michelson interferometer. A Fast Fourier Transform (FFT) of the collected signals would indicate the beat frequency which corresponds to the location of the target. The time delay (τ) is equal to 1/*f*, and the FFT of the frequency sweep gives *R*. The technique can even be applied to identify multiple targets. In this case, the FFT spectrum will show up multiple frequency components corresponding to reflection from each target. This method was used to a greater extent throughout the study and will be discussed later.

2.5 Refractive index determination

The optical path length (OPL) of an electromagnetic wave through a medium of thickness "t", with a refractive index of *n*, is given by

$$OPL = n \times t \qquad (2.13)$$

The Michelson interferometer can be used to determine the refractive index of a sample of known thickness (*t*). This is done by placing the sample in one of the arms between the beam splitter and mirror. The sample introduces an extra path length of $(n-1) \times t$ into the system, resulting in a change in the frequency ω in Equation 2.10 of the interference pattern. This change in frequency, compared to the frequency without the sample is used for calculating the refractive index of the material and is given by [14]

$$n = \frac{\Delta\omega C}{4\pi t} + 1 \qquad (2.14)$$

where $\Delta\omega$ is the change in frequency when the sample is introduced, compared to the frequency without the sample. This change in frequency is determined using equation 2.9 by relating to the optical path difference, when frequency (υ) of the coherent source is swept of a given bandwidth.

Chapter 3

Experiment

This chapter discusses the experiments that were performed utilizing FMCW techniques for determining the spatial (longitudinal) depth resolution and sensitivity. All the systems were designed using a Michelson interferometer and frequency multiplication techniques were used in order to obtain the desired THz frequencies. Data collection techniques used in the study and analysis of the data will also be discussed.

3.1 Initial experiment for target detection

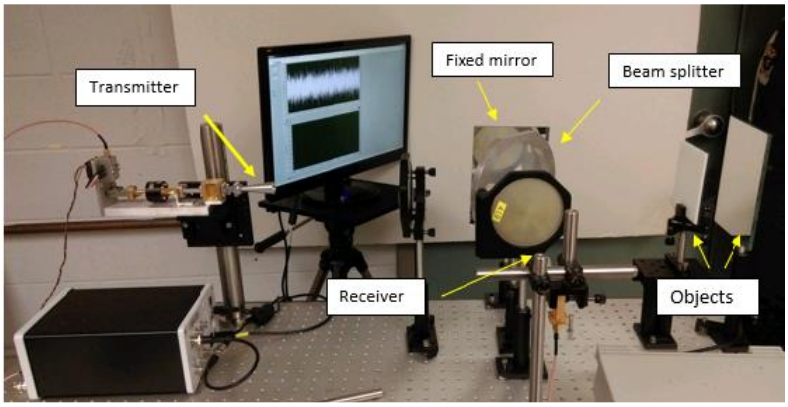

Figure 3.1: Initially developed system that was based on a Michelson Interferometer. mmW/THz frequencies were generated using frequency multiplication techniques. This system could operate between ~72-120 GHz.

Figure 3.1 shows the initial system developed to perform the experiment for target detection. This set up is identical to the basic Michelson interferometer explained in chapter 2.1 (Figure 2.1). The system consists of two mirrors; a fixed and a moveable mirror and a Mylar beam splitter (7 mil) alongside two HDPE collimating lenses for the transmitter and the receiver. The signal is emitted through a conical horn antenna and it is split at the beam splitter where the two beams travel along different paths before they are recombined and detected at the receiver. This is one of the several systems that was developed and tested for the study.

3.1.1 Equipment

A brief description of the equipment used for the experiment is given below. In addition to the apparatus mentioned above, the setup includes a signal generator, a frequency multiplier, a pre amplifier, several optical components (beam splitter, lenses, mirrors) and a data acquisition system (pre-amps, lock-in amplifiers, and National Instruments DAQ cards).

BNC 845 microwave signal generator

Berkeley Nucleonics Model 845 RF Microwave Signal Generator is a low-noise and fast-switching microwave signal generator capable of generating frequencies up to 20 GHz. It can perform various modulations such as frequency, amplitude, pulse and phase. This signal generator was used in the study for FMCW techniques as well as for amplitude

modulation. The signal generator was controlled using a graphic user interface (GUI) designed by the manufacturer.

The instrument can perform frequency modulation either internally or externally. Internal modulation has a maximum bandwidth of 100 MHz which when combined with the frequency extension module that extends the frequency and bandwidth by a factor of 12, as discussed below, corresponds to a range bin of 6.25 cm.. The external modulation mode can sweep a bandwidth up to 900 MHz × 12 = 10.8 GHz, resulting in a theoretical range bin of about 7 mm.

A Mylar beam splitter (7 mil) was used to split the emitted wave (~50/50) so that each wave travels through a different path before getting reflected from the mirrors and two focusing HDPE lenses were used to collimate the signal at the transmitter and the detector. Each lens had a focal length of about 20 cm.

80-120 GHz Frequency Extension Module (FEM) from VDI

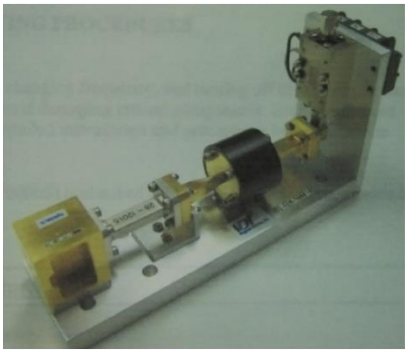

Figure 3.2 VDI 80-120 GHz Frequency Extension Module used in the experiment for frequency multiplication from 6-10 GHz source.

A frequency extension module is an amplifier/multiplier chain series that provides millimeter signals. The module used contains two separate frequency multipliers; active ×4 frequency multiplier and a WR9.3×3 frequency tripler. The active ×4 frequency multiplier requires a 5 V DC power supply and is driven by an input power of 5-8 dBm over 6.7 -10 GHz range by the BNC 845 microwave signal generator. The WR9.3×3 frequency tripler does not require external biasing. This combination extends the signal generator frequency by a factor of 12. Frequency range used for this experiment was from 72 GHz to 120 GHz with output powers of ~1-5 mW over this range.

Zero-Biased Detector (elva-1 ZBD12)

Zero Biased Detectors (ZBD) offer many advantages over traditional detectors [15] the main advantage is the high sensitivity to small signals. They do not require biasing and have a linear response up to -15 dBm (33 μW). The detector used in the experiment has a frequency response range from 60 to 90 GHz with a typical sensitivity of 1700mV/mW at -20 dBm (10 μW) input.

SR560 Low noise pre amplifier & the data acquisition (DAQ)

The Stanford Research 560 is a high-performance, low-noise preamplifier with a wide variety of applications in different branches. This pre amp was used to amplify the signal at the receiver and has DC/AC coupling modes along with low and high pass filtering capabilities. The DAQ system used in this experiment was a National Instrument USB -6216 with a maximum acquisition rate of 10^5 data points/sec (10 kHz) and a 16-bit resolution. Two channels were used; one of them was the analog signal from the pre-amp

and the other was the modulated signal from the function generator. For the experiment, the maximum data acquisition rate was used and the number of data points collected with this rate varied from 10,000 to 100,000.

3.1.2 Method

A signal (CW) with carrier frequency of 7.5 GHz from the BNC synthesizer, internally modulated with 100 MHz triangular wave, was passed through the frequency extension module (FEM) which multiplied the frequency by a factor of 12, to 90 GHz with a modulation span (bandwidth) of 1.2 GHz. A triangular wave was swept at a rate of 100 Hz. This FMCW signal travels through the Michelson interferometer, gets split at the beam splitter, reflects from the mirrors and reaches the detector with interference information embedded in it. The received signal was passed through the SR560 preamplifier with AC coupling to improve the signal to noise ratio. Data collection was carried out through a Labview program using the DAQ system mentioned above and both the interferometer signal and FMCW ramp were digitized.

Data analysis is based on extracting the interference cosine term of equation 2.9 that determines target location precisely. This interference term is derived through a normalization procedure and is fitted with a cosine function as described in chapter 2, which gives the target location. To extract the interference term, three separate pieces of information are needed; intensities of near and far arms and both arms together. Data from individual arms were collected by covering the other arm with an echo-absorber. As will be shown in the next section, the reason these steps were taken is to improve the quality of the data by extracting the interference term from equation 2.9, due to the

variations in I_1 and I_2. This approach allows us to fit equation 2.9 to the relevant parameters we are interested in.

3.1.3 Results

Data analyzed through Igor pro is shown below. Figures 3.6, 3.7 and 3.8 are the signals from far, near and both arms respectively. Far and near arms were located 25 cm and 10 cm respectively from the beam splitter and these signals are related to reflections off each arm. 100,000 data points were collected at an acquisition rate of 10^5 data points/second resulting in a frequency sweep of one second duration as shown on below graphs.

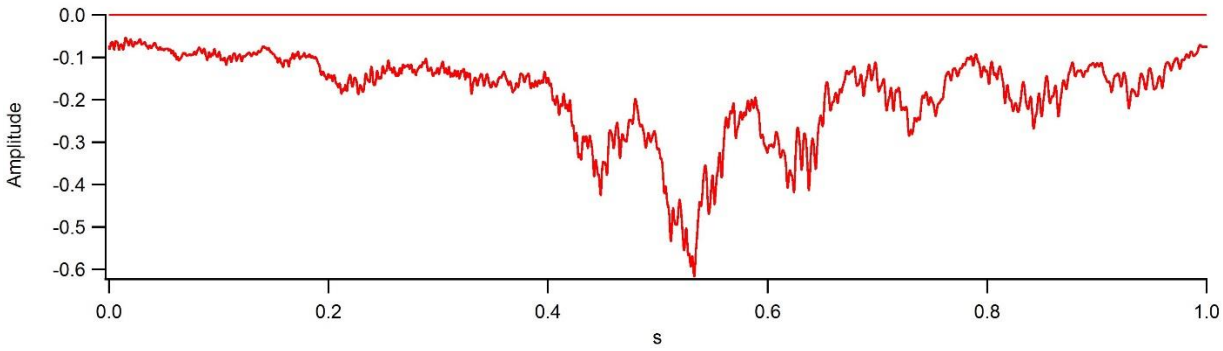

Figure 3.3: Signal collected from far arm (I_1) with a 1s sweep.

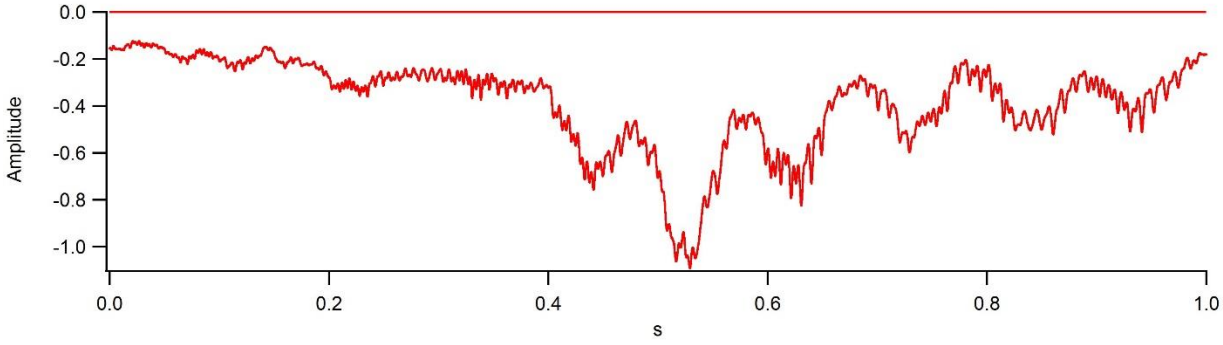

Figure 3.4: Signal from near arm (I_2).

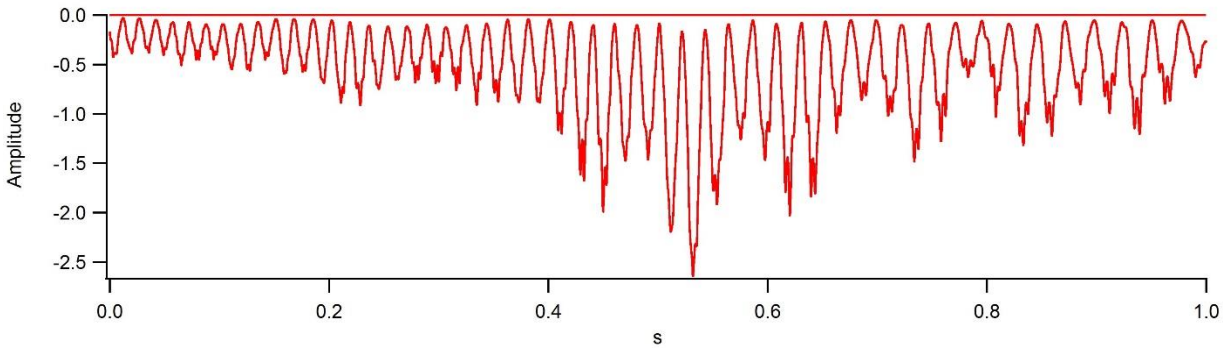

Figure 3.5: Signal from both arms (*I*) with the interference pattern.

The amplitude change in signals is due to the power variation of the transmitter over the frequency range of interest. The signal collected with both arms open (Figure 3.5) has a clear interference pattern where the minimas have almost zero amplitude. A reference line across zero amplitude has been drawn on all three Figures, to help in better visualization.

Next, the visibility function (V) was derived using the relationship;$V = \frac{2\sqrt{I_1 I_2}}{I_1 + I_2}$. If $I_1 = I_2$, then the visibility function (V) = -1 This negative value of V instead of +1 is an artifact due to the negative voltage detected by the diodes. The visibility function for the above data is shown on Figure 3.6.

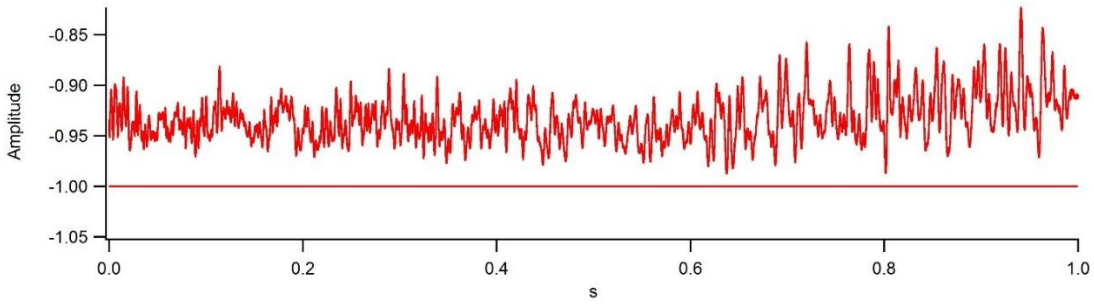

Figure 3.6: Visibility function (V) obtained by combining intensities of both arms.

Finally, the cosine term was extracted using the equation (Figure 3.7);

$$cos(\Delta\phi) = \frac{\frac{I}{I_0} - 1}{V} \qquad (3.1)$$

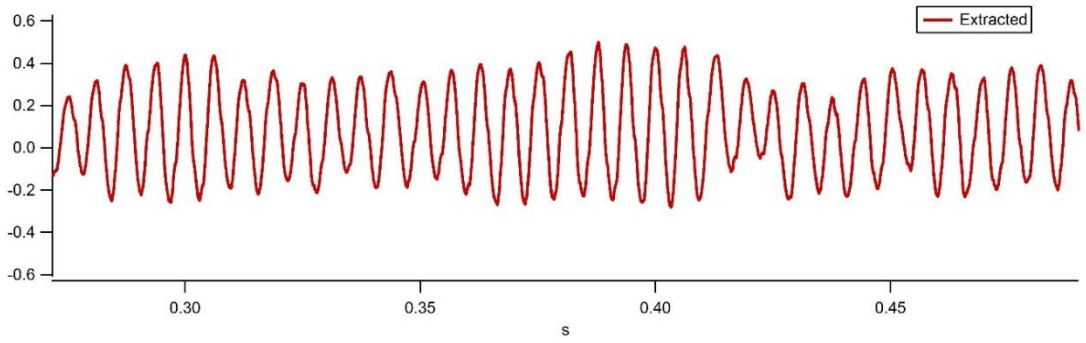

Figure 3.7: Extracted cosine function through the normalization procedure (whole range not displayed).

We perform a cosine fit for the extracted cosine term and this leads to obtaining the FFT peak corresponding to the path difference between the two arms of the Michelson interferometer. Figure 3.8 shows the fitted cosine function to the extracted cosine function. The fitted function is of the form

$$f(x) = y_0 + A\cos(fx + \phi) \qquad (3.2)$$

Obtained parameters and their uncertainties are given below

y_0	A(V)	f(Hz)	ϕ
0.048 (2)	0.56 (2)	3.7282e-9 (1)	1.28 (3)

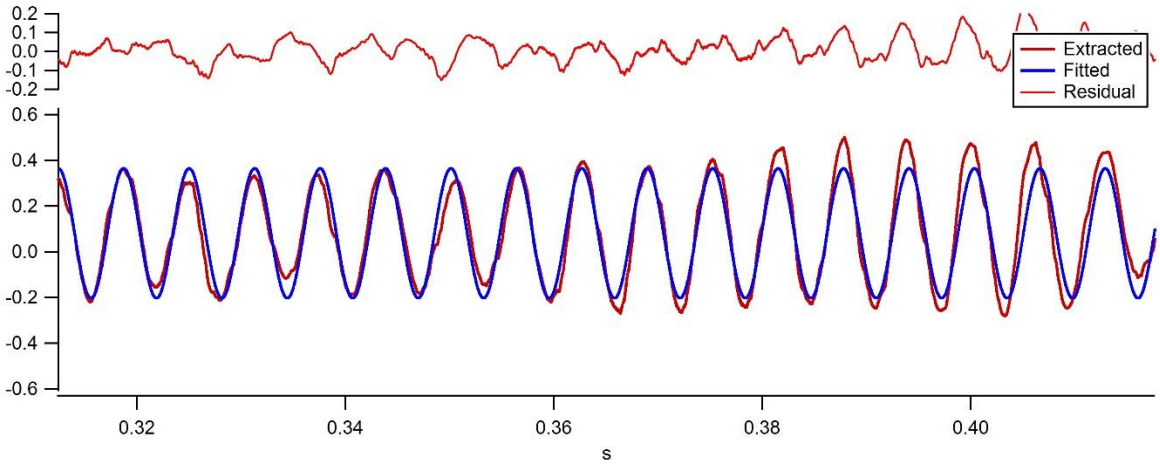

Figure 3.8: Cosine function fitted for the extracted function using a fitting tool in Igor pro, with the residual of the fit on the top graph (whole range not displayed).

The FFT of the fit closely matches the peak related to extracted cosine function, as in Figure 3.9. Curve fitting tool in Igor-pro was used for performing the fits.

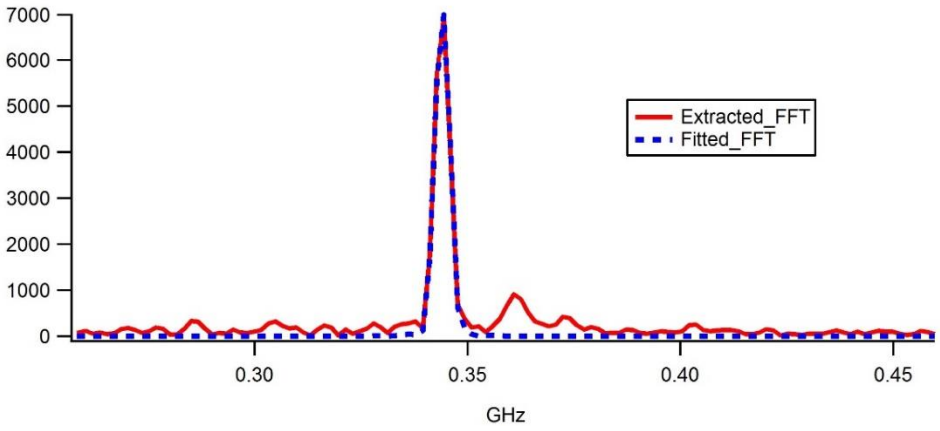

Figure 3.9: FFT of the extracted and the fitted cosine function. The axis units in this case have not been scaled to the range and represent the units associated with the FFT.

Instead of observing the path difference between the two arms, it was convenient to represent the distance to one of the arms of the beam splitter. So, the distance of interest is taken to be from the far arm to the beam splitter. Far arm was physically measured to be 37 cm (1) from the beam splitter and the interferometrically measured value is 37.67 cm. This measurement is done by converting the frequency space in the FFT to an optical path difference that will be discussed later in chapter 3.23.

Theoretical resolution for this system, calculated from the bandwidth of the sweep, is about 6.25 cm and the next task was to improve the resolution of the system, since we were interested in millimeter range resolution of multiple targets. Resolution is hindered by the internal modulation of the synthesizer which is limited to 100 MHz. So the system had to be modified by means of external modulation via low frequency (LF) output of the synthesizer. External modulation can sweep a bandwidth up to 900 MHz × 12 = 10.8 GHz, resulting in a resolution of about 7 mm. There are two ways to externally modulate the signal; it could either be done using the internal function generator in the BNC 845 synthesizer (via external connections on the back panel from FUNC OUT to ΦM) or using an external function generator. Both supply a FM waveform voltage to ΦM and the sweep bandwidth sensitivity in Hz/V could be set via the BNC interface software. This permitted a larger bandwidth (900 MHz).

Several experiments were performed using both an external function generator and the internal function generator in the BNC 845 synthesizer into the external modulation connection, ΦM. While using external modulation and carrying out the same data collection and analysis procedure, it was observed that the frequency sweep deviated from linearity leading to a noticeable deviation in the fitted cosine function from the

original function (Figure 3.10). This resulted in the FFT peak of the fitted function being shifted from the FFT peak of the extracted signal and a significant broadening of the FFT of the extracted signal, shown in Fig. 3.11.

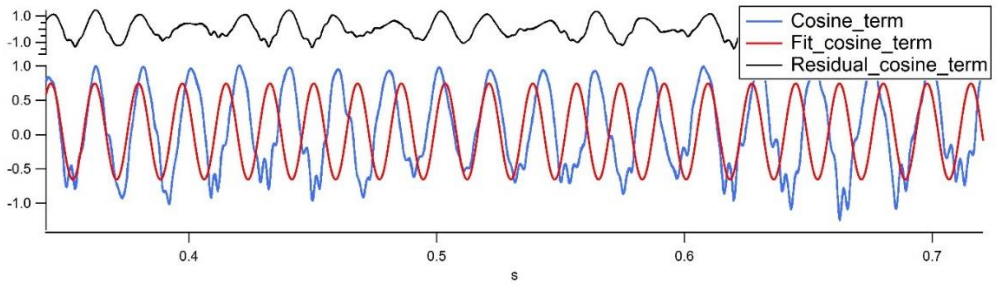

Figure 3.10: Extracted cosine function vs the fitted cosine function (whole range not displayed)

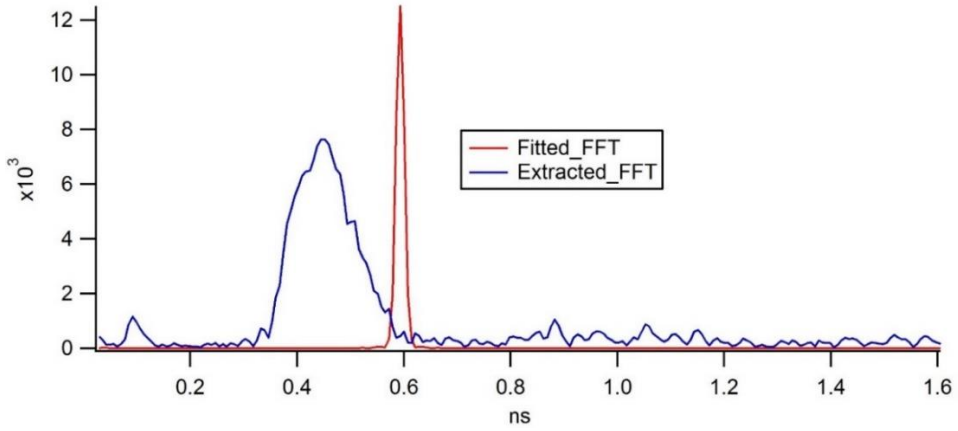

Figure 3.11: Fitted and the extracted FFT peaks. There is significant broadening in the extracted FFT

This deviation from expected results could be due to multiple factors. One factor could be the result of non-linearity of the frequency extension module due to power variation in the frequency sweep. Specifically, the interference pattern could become distorted since

the output power of ~1-5 mW of the transmitter is above the -15 dBm (33 μW) linearity threshold of the ZBD detector/receiver over the much larger 10.8 GHz sweep bandwidth. Partial saturation of the detector signal above this threshold could cause a distortion in the interference pattern, particularly since the power varies over the sweep. To examine the power variations over the operation range of the system, the following method was used. A Labview program was created to amplitude modulate the frequency from 72 GHz to 120 GHz in increments of 0.001 GHz and used with a lock-in amplifier. System was driven at 5 dBm by the synthesizer, a slightly lower setting than 8 dBm and consequently a lower output power (but this was not quantified) and signal was collected with both arms opened (Figure 3.12). The lower output power, the small steps in frequency, and wanting to quantify the variations of the output power through AM modulation was the reason the lock-in amplifier was used. The relative output power of the transmitter is shown in Fig. 3.12.

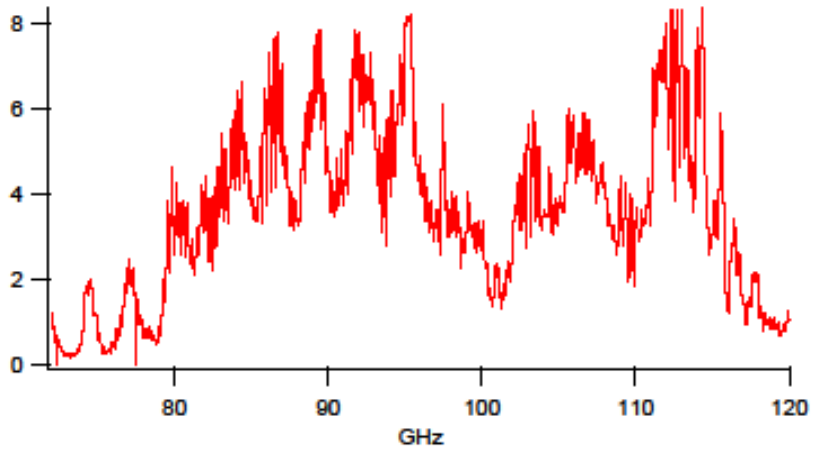

Figure 3.12: Power variation in the system from 72 GHz to 120 GHz. The synthesizer output at 5 dBm.

Frequency sweep in the internal modulation at 100 MHz was observed through the fits to be linear from 90 GHz to 91.2 GHz. So this frequency range was extracted from the above signal and was used to normalize the raw signal. It was expected that this process would remove any factors causing non linearity in the sweep. This method could also be applied at regions with lower output powers that would avoid detector saturation and distortion of the interference pattern. However, results of the analysis did not indicate any relationship between the power variation and non-linearity of the sweep. Several attempts were made to linearize the sweep over the range of interest and none of them were successful. The most likely reason for the non-linearity is not the detector saturation, but noise on the FM waveform voltage used to sweep the BNC frequency, particular since the sweep bandwidth sensitivity in Hz/V was maximized to maximize the sweep bandwidth for a given voltage. This prompted switching to a different system that was capable of a large bandwidth linear sweep rather than trying to linearize the sweep of the initial system.

This new system was based on an early work carried out to determine refractive indices of dielectric materials [14]. The system consisted of a YIG based voltage controlled oscillator (VCO) that swept from 20 – 40 GHz with a control voltage of 0-10 V (2 GHz/V). This signal was fed to a $(\times 6)$ VDI multiplier chain and the frequency sweep carried out, was a combination of amplitude and frequency modulations.

3.2 New experiment

3.2.1 Experimental Setup

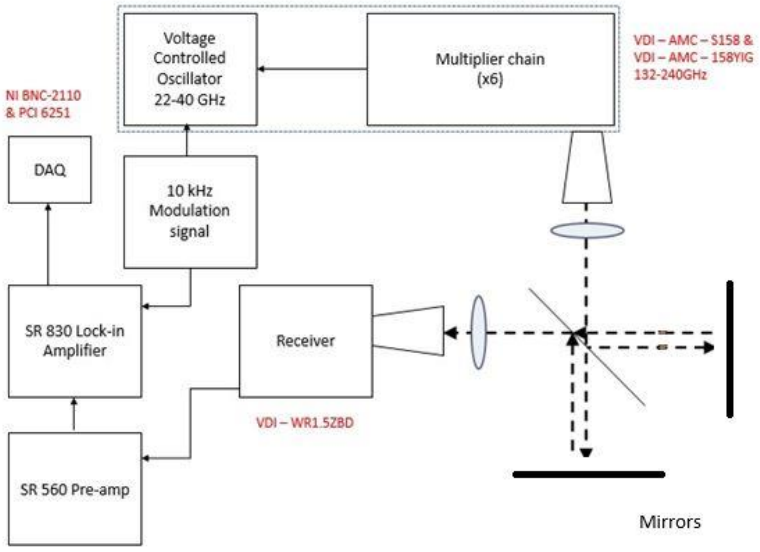

Figure 3.13: The setup with a 22-40 GHz VCO as the THz generator.

VDI -AMC-S158 is a YIG voltage controlled oscillator that generates 22-40 GHz with a control voltage of 1-10 volts. VDI-AMC-158YIG increases the frequency by a factor of 6 through a multiplier chain. The signal is AM modulated by a 10 kHz square wave and the received signal passes through an SR560 pre amp with its gain set to be at 20, before being passed through the SR830 Lock-in amplifier.

This system sweeps from 132 GHz to 240 GHz and the data collection process was automated using a Labview program. Same data collection and analysis procedure as in the earlier experiment was carried out and the frequency sweep was observed to be highly linear over the entire range of sweep than the previous system.

Initial experiments were performed by moving the far arm mirror by a known distance. A shift in the FFT peak related to the reflection from the mirror is expected as its being moved. The far arm mirror in the Michelson interferometer was mounted on a LabVIEW controlled Anaheim linear stage (www.anaheimautomation.com) where movements were determined with extreme precision to about 10 μm.

Starting from a measured initial position, intensities of the far arm, near arm and both arms were collected to extract interference information via the visibility function. Then the far arm mirror was moved by a known distance from initial position and the same data collection was performed. Separation between the initial and final positions of the mirror was experimentally determined and compared with the known displacement, based on the resolution criteria mentioned below.

3.2.2 Resolution criteria for FFT method

There is a minimum resolution criterion for distinguishing two peaks based on full width at half maximum (FWHM) of each peak. If the peak separation is greater than FWHM, the 2 peaks are considered to be resolvable.

Spatial depth resolution depends on bandwidth of the sweep as discussed before and for the system used, which has a bandwidth of 108 GHz, has a theoretical resolution of about 1.39 mm. This is valid if the interference pattern is acceptable in the entire swept region as the sweep bandwidth (B) is mathematically related to the FWHM of the FFT. But the observed interference pattern was not linear at the beginning and ending stages and therefore not included in the analyzed data, which makes the bandwidth of the sweep slightly smaller than 108 GHz, resulting in a value larger than 1.39 mm.

3.2.3 Conversion of frequency to optical path difference

During data collection process, frequency was swept from 132 GHz to 240 GHz for a bandwidth of ~108 GHz. The FFT data has a temporal increment that is the inverse of the bandwidth. The temporal space can be converted into an optical depth by taking into consideration the time delay of the *reflected* signal. So the theoretically resolvable path difference is equal to temporal increment times half of speed of light, i.e. Eq. 2.12. The above bandwidth has an equivalent temporal increment of 9.259×10^{-12}s and a corresponding spatial increment of 1.4 mm. This scale was used to represent the graphs through Igor-pro.

3.2.4 Padding the FFT

Zero padding is the process of adding zeros to end of a time-domain signal to increase its length. Padding the FFT visually improves the signal by adding extra data points and creates a smoother (interpolated) FFT. Figure 3.14 compares the FFTs with and without padding. Also, a Hanning window function was used while performing the FFT. Original data consisted of 200000 data points and FFT without padding contained 100001 data points while the padded FFT consists of 131073 data points. Addition of extra data points changes the frequency increment, so this factor needs to be considered when converting to an optical path difference.

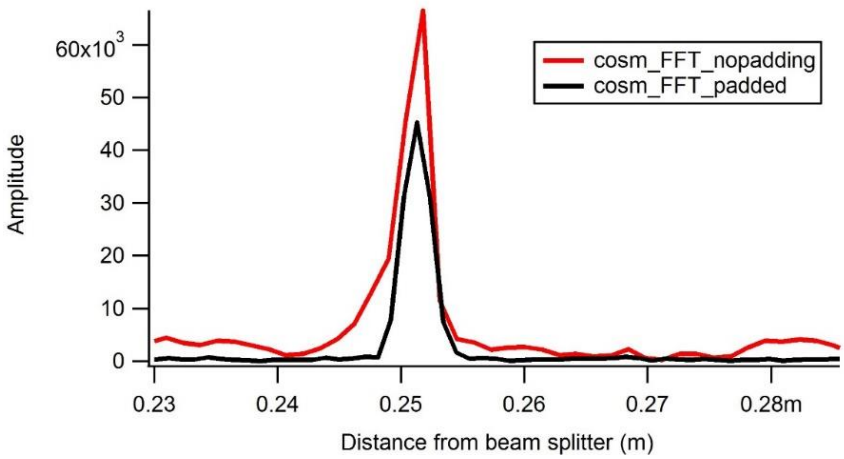

Figure 3.14: FFTs with and without zero padding. This process makes the FFT peak symmetric while preserving the center of the peak of the original FFT.

Padding the FFT also helps to fit a smooth Gaussian curve for the peak, thus reducing the uncertainty in determining the peak. Figure 3.15 shows the padded FFT with a Gaussian curve fitted. x0 is the location of the peak in the Gaussian curve.

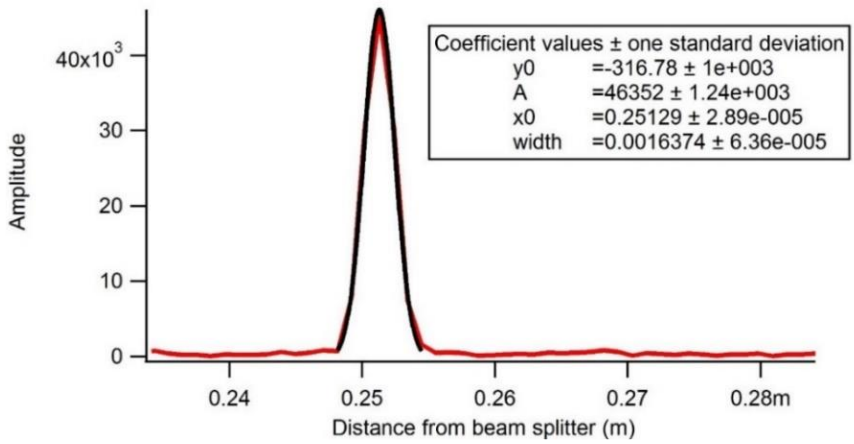

Figure 3.15: Padded FFT with a Gaussian fit to accurately determine the peak location.

3.2.5 Test of the accuracy of the calibration

Distance to the far arm from the beam splitter was interferometrically measured and was compared with the physically measured distance. The calibrated distances from experimental results agrees with measured distances based on their uncertainties. Distances between the beam splitter, far and near arms were measured using a meter stick which carries an uncertainty of ±0.5 mm. It was approximated that the uncertainty in determining the location of the beam splitter to be ±0.5 cm. The experimental uncertainty is given by the uncertainty in the peak of the FFT. The results for measuring the distances from the beam splitter to the far arm is:

Measured distance = $25.0 \pm 0.5\ cm$ (2 %)

Experimental = $25.129 \pm 0.003\ cm$ (0.01 %)

Percent difference = 0.48 %

3.2.6 Results for displacement measurements

Following results are for two separate movements of the mirror done by a linear stage; 1 cm and 1 mm. Optical path differences were measured from the beam splitter, but we are interested in determining the difference in the mirror's location as moved by the linear state, that has an accuracy on the order of 10 μm.

Displacement resolution test of 1 cm

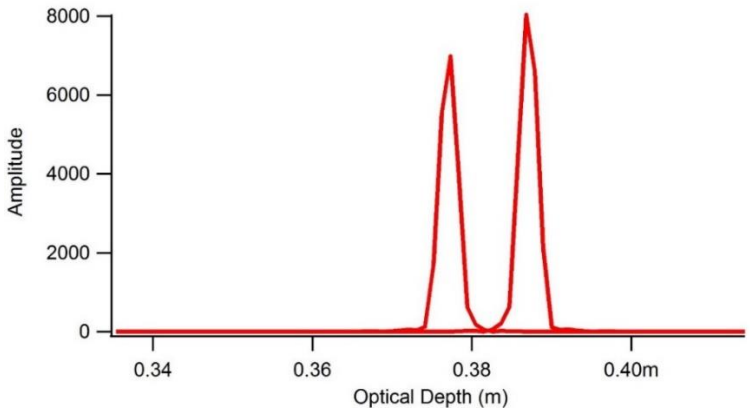

Figure 3.16: Mirror displacement of 1 cm. These 2 peaks correspond to two separate data collections.

To accurately determine the peak location of the data shown in Fig 3.16, Gaussian functions were fitted (shown in Figure 3.17) and their Full Width at Half Maximum was found using the following relationship

FWHM= 1.665095 × Gaussian width

where the Gaussian width is a parameter in the Gaussian curve fit equation in Igor Pro given below

$$y_0 + Ae^{\left\{-\left(\frac{x-x_0}{width}\right)^2\right\}} \qquad (3.3)$$

Based on fitting the peaks to this equation, FWHM was determined to be 0.27 cm for each peak.

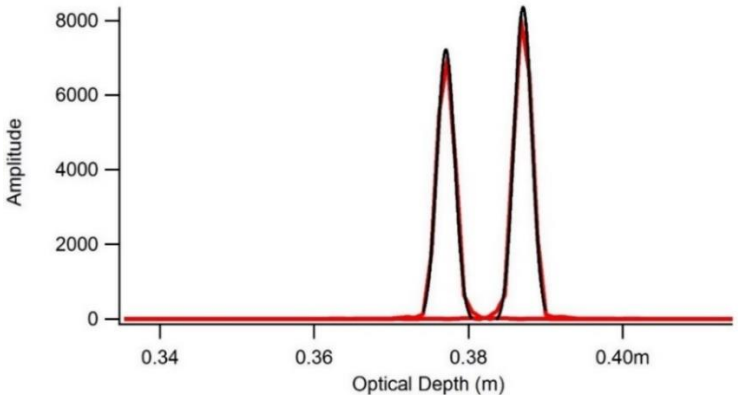

Figure 3.17: Gaussian fits for the peaks associated with 1 cm movement of the mirror mounted on the linear stage.

The separation of peaks (1 cm) is greater than FWHM for the peaks, therefore these peaks are easily resolvable. The displacement of the mirror by the linear stage was 1 cm and the experimentally measured separation is $1.001\ cm \pm 70\ \mu m$ which is very close with an error of 0.1 %, near the ~10 μm resolution of the stepper motor that moves the linear stage.

Displacement resolution test of 1 mm

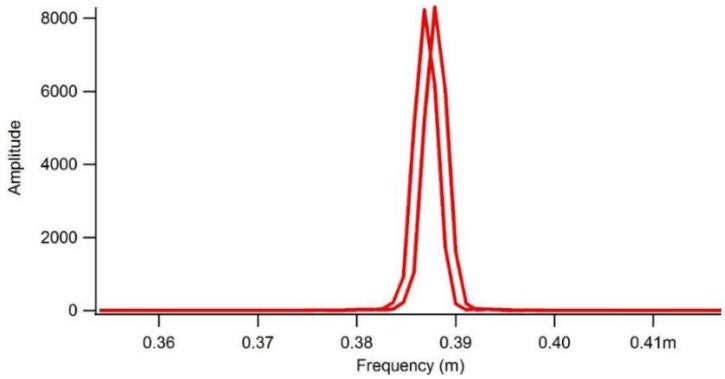

Figure 3.18: Mirror moved by 1 mm. The FFT peaks are much closer to each other compared to 1 cm mirror displacement.

Similar to the last resolution test, the linear stage was used to move the mirror by 1 mm to allow a comparison of the two FFTs to determine if this displacement could be resolved is shown in Fig 3.18. In this case, the experimental peak separation was determined to be 1.02 mm. While this is a 2% difference in the displacement of the linear stage, the absolute difference is only ~20 microns, which is close to the stepper motor resolution.

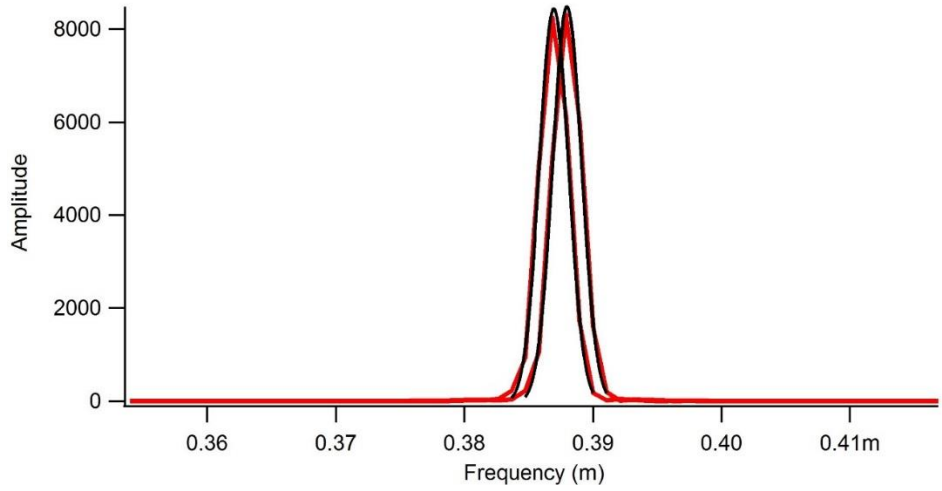

Figure 3.19: Gaussian fits for the peaks at 1 mm. Based on the resolution criteria, they are just resolved.

For both peaks, the FWHM was determined to be 0.27 cm for each peak. This is same as the value obtained for 1 cm mirror displacement. It is clear that an individual mirror's displacement can be tracked very accurately on the order of ~10-50 microns. However, the separation of peaks is less than FWHM=2.70 mm. Therefore these two peaks can be defined as unresolvable even though there is a measurable displacement shift.

Consequently, if two targets or surfaces of two targets are separated by less than FWHM, they would not be distinguishable.

Results of this experiment verifies the dependence of spatial resolution on the bandwidth of the frequency sweep. 1 mm separation of two surfaces demonstrates that an induvial surface can be track to better than the range resolution ($c/2B$) of 1.39 mm. However, two surfaces would not be resolvable based on the resolution criteria of being separated by the FWHM of the Gaussian profile, which is approximately twice the range resolution. The uncertainty of an FFT can be considered to be the theoretical resolution of the system which is ± 1.4 mm.

3.3 Resolving multiple interfaces (HDPE plate and a mirror)

As an experimental test of the FWHM system to resolve multiple surfaces, this section presents results of a 3.05 mm HDPE sample placed in front of a mirror. The Frequency region used for the study is transparent to HDPE, so, substantial amount of signal passes through the sample. Separate sets of data were collected without the sample and with the sample in front of mirror. Again, Gaussian curves were fitted for all relevant peaks to determine their locations.

Figure 3.20 shows the FFT peak with only the mirror being placed at 37.5 cm $\pm$ 0.5 cm from the beam splitter. Observed peak is at 37.67 cm $\pm$ 0.008 cm which falls within the uncertainty window.

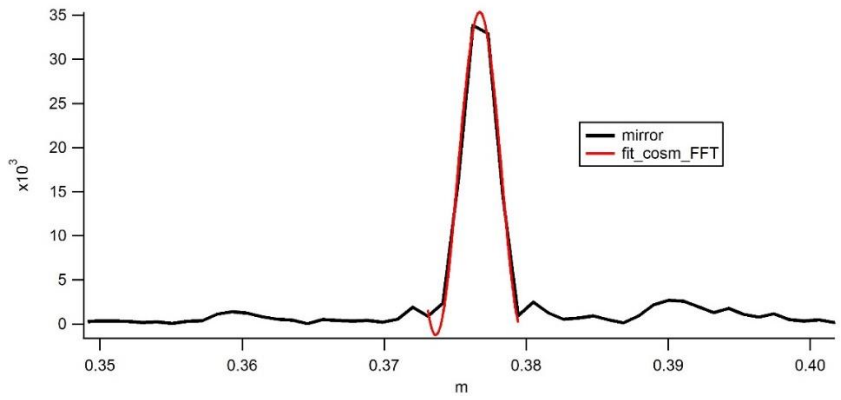

Figure 3.20: FFT peak corresponding to the mirror without the HDPE sample in front. (Vertical axis displays the amplitude of the FFT).

Figure 3.21 shows the FFT peaks of HDPE sample placed in front of the mirror. Physical separation between the mirror and the sample was 1.8 cm. As expected, two distinct peaks corresponding to the front and back surface of the sample is observed, one at a distance 35.4 cm and the other at 36.3 cm from the beam splitter.

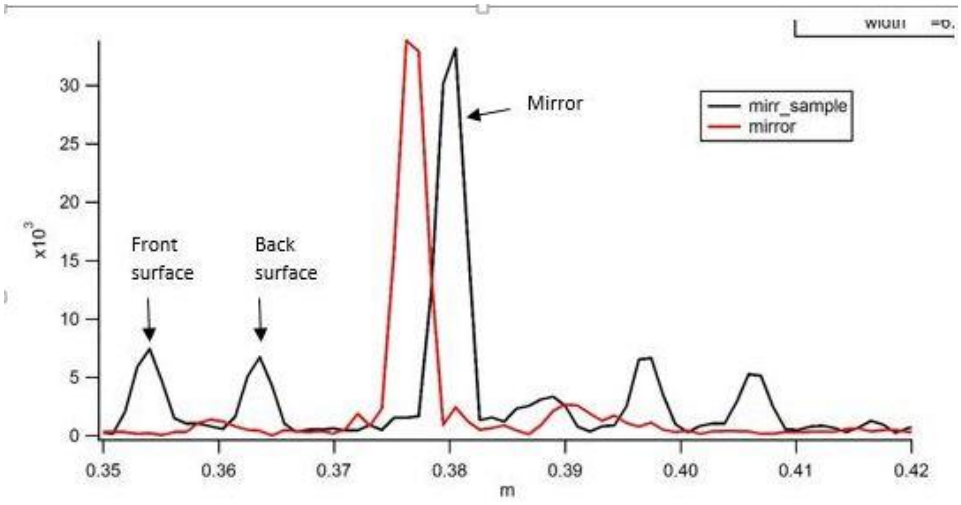

Figure 3.21: Comparison of the FFTs with and without the sample. Peaks related reflections from the front and the back of the sample are clearly visible. (Vertical axis displays the amplitude of the FFT).

The peak related to the mirror is shifted from original position. This is due to the extra path length (n-1)t introduced by the sample, where n is the refractive index of the sample and t is the sample thickness. There are distinguishable peaks behind the mirror with separations similar to the peaks from front and back of the sample. These are due to multiple reflections off the other side of the sample.

Given below are locations of each peak calculated from the beam splitter and based on the Gaussian fits of the peaks.

Mirror= 38.005 $\pm$ 0.002 cm

Front Surface of the sample= 35.402 $\pm$ 0.002 cm

Back surface of the sample= 36.355 $\pm$ 0.002 cm

These experimental peak locations agree well with the physically measured locations. Based on these results, it is possible to resolve reflections from multiple targets, or surfaces and sub-surfaces, and hence accurately determine their locations. These results are also consistent with the sample thickness and the index of refraction (overall optical path between the interfaces of the sample) that is determined in a later section.

3.4 Resolving multiple interfaces – two HDPE plates

The sample used for this experiment is formed by combining two HDPE plates with thicknesses of 6.336(2) mm and 3.052(3) mm as shown in Fig 3.22. An intentional air

gap effectively paves the way to four reflections from the front and back of each layer as shown in Figure 3.23. Refractive index of the HDPE is required to mathematically calculated the optical path length.

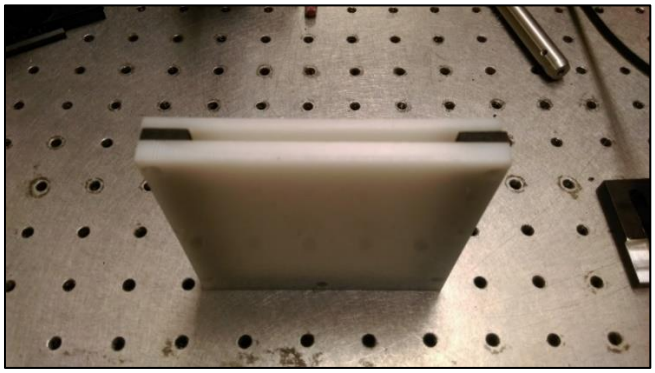

Figure 3.22: Combined HDPE sample with an air gap.

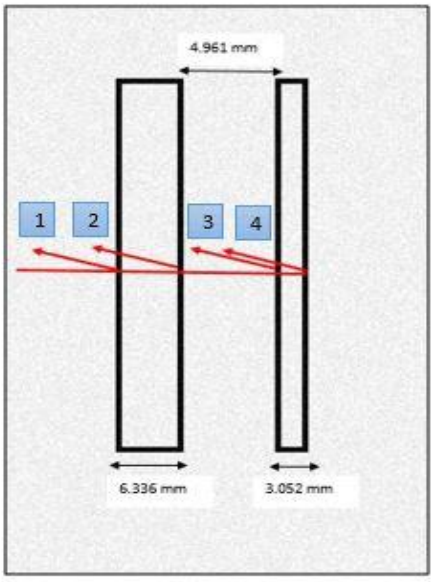

Figure 3.23: Illustration of reflections from each interface.

3.4.1 Setup

The sample was used as the far arm of the Michelson interferometer by placing a millimeter-wave echo absorber behind it. Reflected signals from each arm as well as both arms together were recorded. Signal strength of the sample detected from the SRS lock-in amplifier was observed to be weak, and therefore its sensitivity was reduced to 5 mV as compared to the initially set value of 500 mV (i.e. amplifier gain increased by a factor of ten), when collecting data. Later, it was rescaled to match the original sensitivity. Representative data is shown in Fig 3.24.

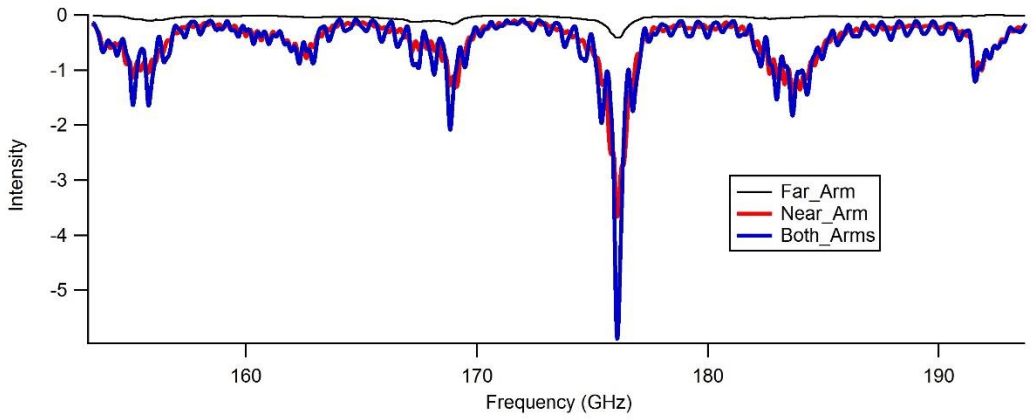

Figure 3.24: Raw signals from collected from far, near and both arms.

3.4.2 Analysis

Extraction of interference information was carried out using the visibility function (chapter 2) and four peaks were clearly noticeable on the FFT of the normalized cosine function (Figure 3.25).

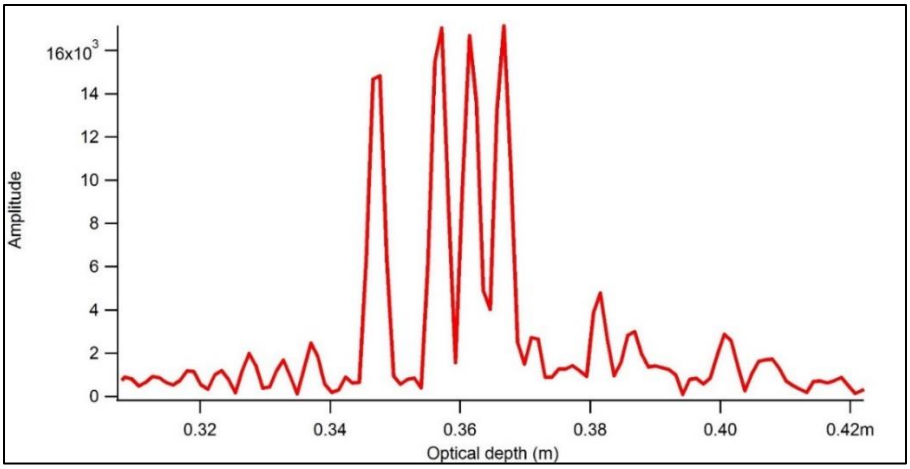

Figure 3.25: FFT of the cosine function shows distinct peaks that agree with physically measured separations between them.

Since the FFT peaks were not smooth, a Gaussian function was fitted for each one to determine the location of peaks. The following peak locations were measured from the beam splitter.

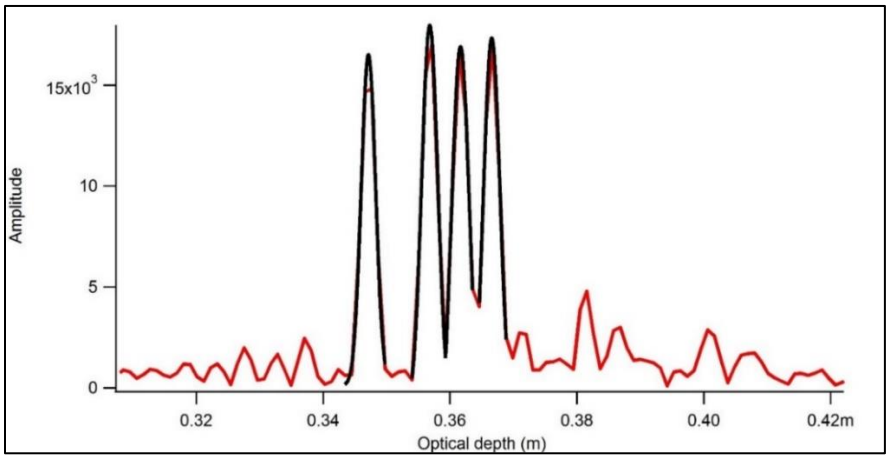

Figure 3.26: Gaussian fits for each FFT peak.

Peak locations (as in Figure 3.26)

1. $34.714 \pm 0.003\ cm$
2. $35.681 \pm 0.001\ cm$
3. $36.166 \pm 0.008\ cm$
4. $36.658 \pm 0.002\ cm$

The separations between corresponding peaks are compared with physically measured values in the Table 3.1 below. For the first and third separations, these correspond to reflections from the front and back of the samples. The index of refraction of HDPE (n_{HDPE}=1.5355) determined in a later section was multiplied by the physical measurement so a comparison to the interferometically measured values could be made. Two of the three separations are in agreement.

Interferometrically measured separations (mm)	Physically measured separations (mm) × n
9.67(2)	9.69(1)
4.85(8)	4.96(1)
4.92(8)	4.67(1)

Table 3.1: Interferometrically and physically measured separations (multiplied by the index of refraction).

3.5 Modelling the interference

In this chapter, results of modelling the cosine term which carries interference information, is presented. The model will be compared with experimental results in order to verify and compare its accuracy.

As shown earlier, the intensity of the signal from each arm is given by

$$I(I_1 I_2) = I_1 + I_2 + 2\sqrt{I_1 I_2}\cos(\frac{2\pi}{\lambda} OPD) \quad (3.5.1)$$

In terms of frequency

$$I(I_1 I_2) = I_1 + I_2 + 2\sqrt{I_1 I_2}\cos(\frac{2\pi}{C}(OPD)\,\upsilon) \quad (3.5.2)$$

Where $OPD = 2n(l_1 - l_2)$

Remarks: There is a phase change from each mirror, since the reflection is from the interface of a rare to dense medium. But this effect cancels out in the interference term.

3.5.1 Modelling interference of signals from two mirrors

In this section we compare the extracted parameters, the optical path difference or the distance to the target, by modelling the interference pattern verses identifying peaks of the FFT of the interference pattern. Theoretically they should be identical, but the complex data collected may cause the results to differ.

Here, results are presented for interference using two mirrors located at positions 15.6 cm and 38.5 cm with respect to the beam splitter. Since our experimental sweep is from 132 GHz to 240 GHz, theoretical model was scaled to match the same frequency range.

3.5.2 Theoretical Results

Cosine term associated with interference equation and based on the measurement above is given by

$$Cos(2\pi \frac{2(l_2-l_1)}{C} v) = Cos(2\pi \frac{2(0.229)}{299792458} v) \quad (3.5.3)$$

Below is the graph of above equation plotted using Igor –pro.

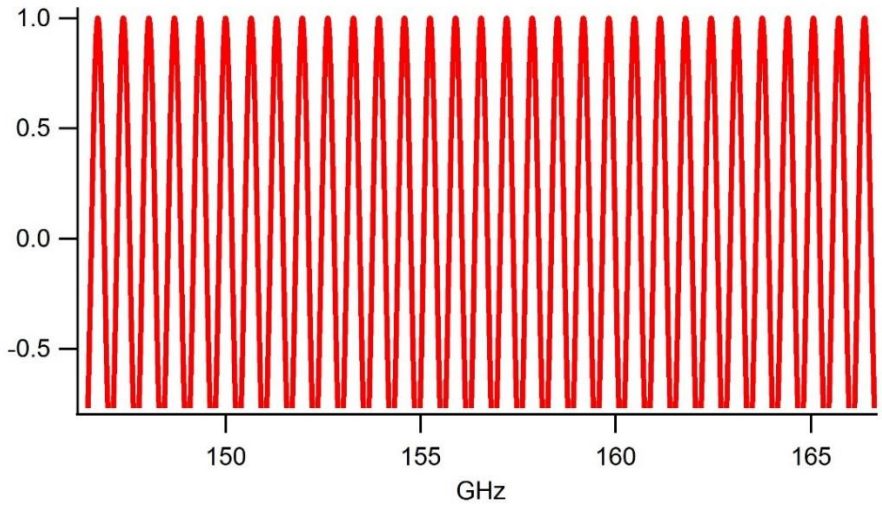

Figure 3.27: Cosine function (whole frequency range not displayed).

FFT of the signal (Figure 3.28) was scaled accordingly and converted to an optical path difference as explained in earlier chapter.

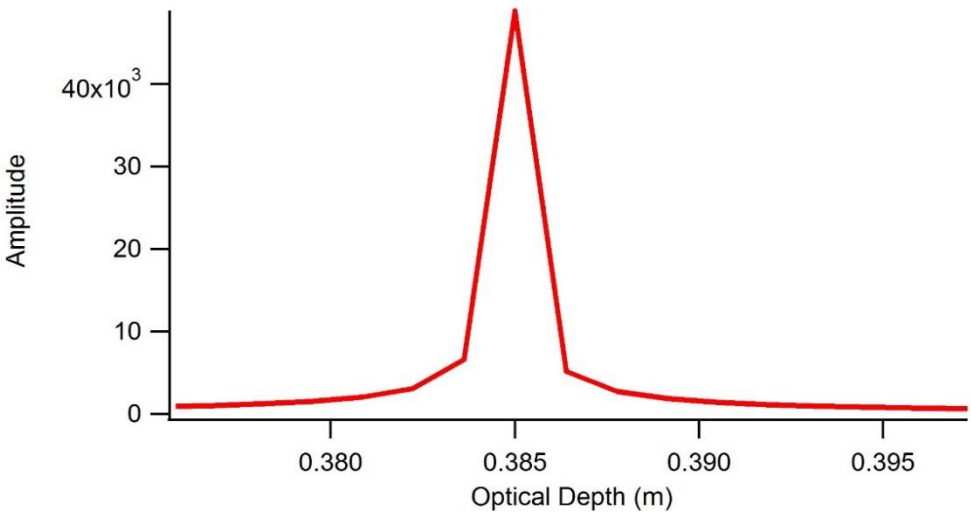

Figure 3.28: FFT of the modelled cosine function.

A Gaussian curve is fitted to the peak FFT in order to determine the peak location.

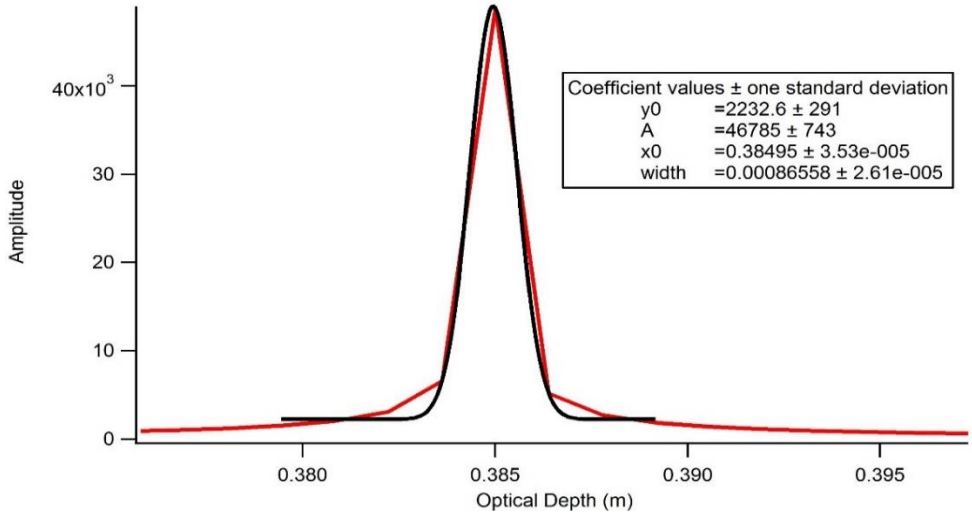

Figure 3.29: Gaussian fit for the peak FFT.

In the interference model, original position of the far mirror was measured to be 38.5 cm from the beam splitter and the value given by FFT after the Gaussian fit is 38.495 cm. So these values are extremely close (50 μm), which verifies the accuracy of the method, as expected.

3.5.3 Comparison with Experimental results

Same procedure was followed for the experimental results and the cosine term was extracted. Figure 3.30 & 3.31 show the experimental cosine function and its FFT.

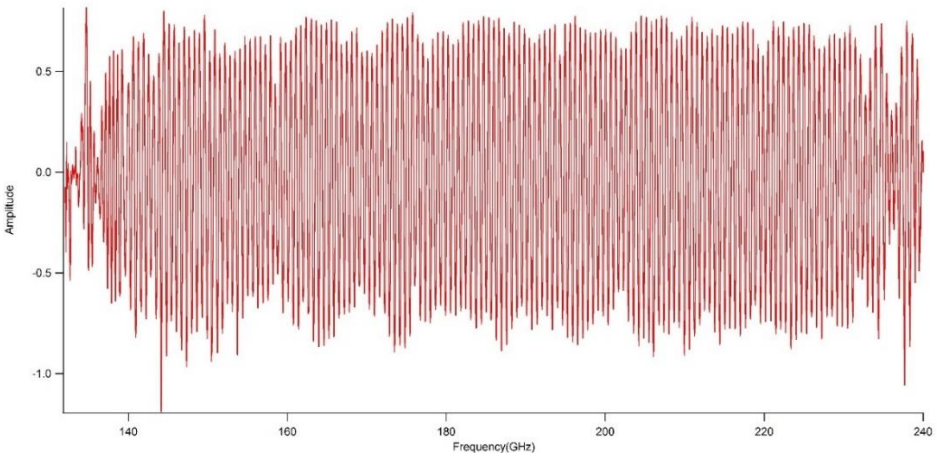

Figure 3.30: Experimental cosine function.

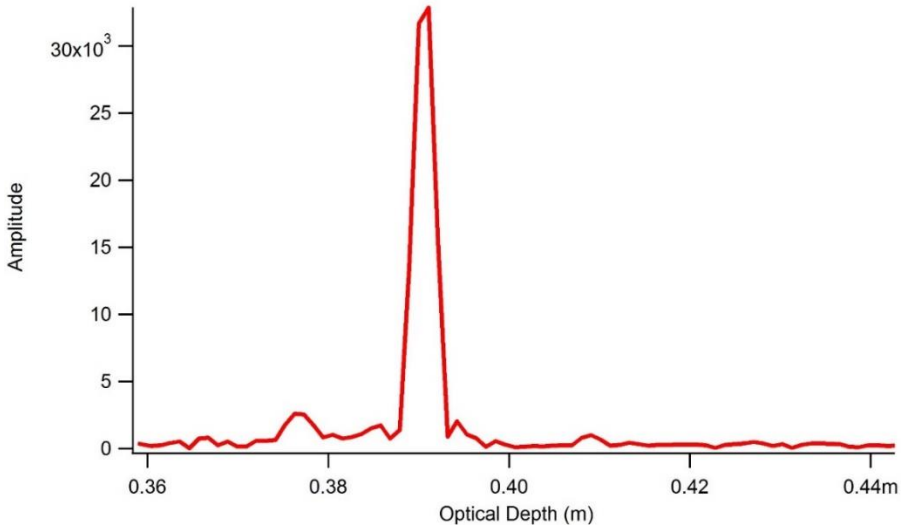

Figure 3.31: FFT of the experimental interference pattern.

Again, a Gaussian curve is fitted to the FFT peak to determine its exact location.

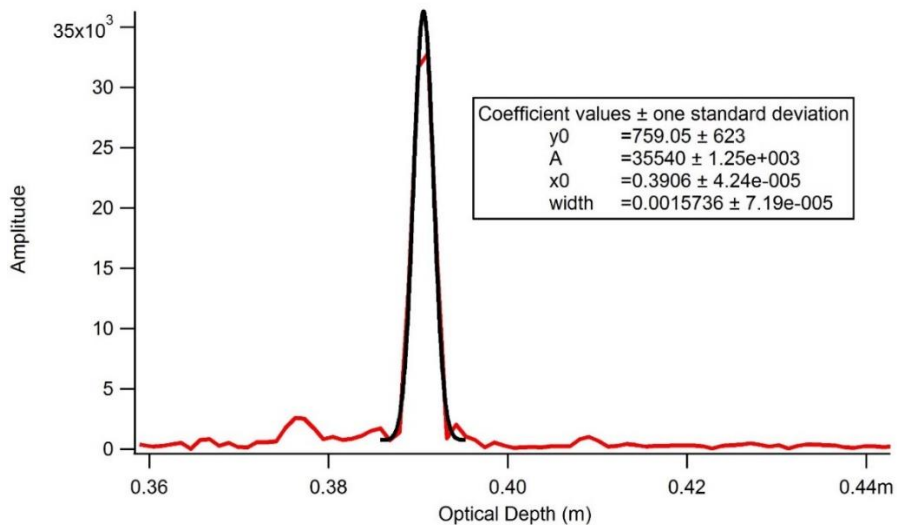

Figure 3.32: Experimental cosine function with a Gaussian fit for the peak.

Next, the model and the experimental results are compared for accuracy. Both peaks look to be fairly close to each other and within the experimental uncertainty of the physical measurements. Determining the location of the beam splitter using a meter stick carries a larger uncertainty than the uncertainty associated with the meter stick itself (~1 mm). This was due to the difficulty in determining the actual beam location and accessing the beam splitters and mirrors with inadvertently moving them out of alignment. As a consequence, parallax error dominated the total uncertainty in determining the location of the beam splitter and mirror, so the uncertainty in the physical measurements is estimated to be no better than ±0.5 cm.

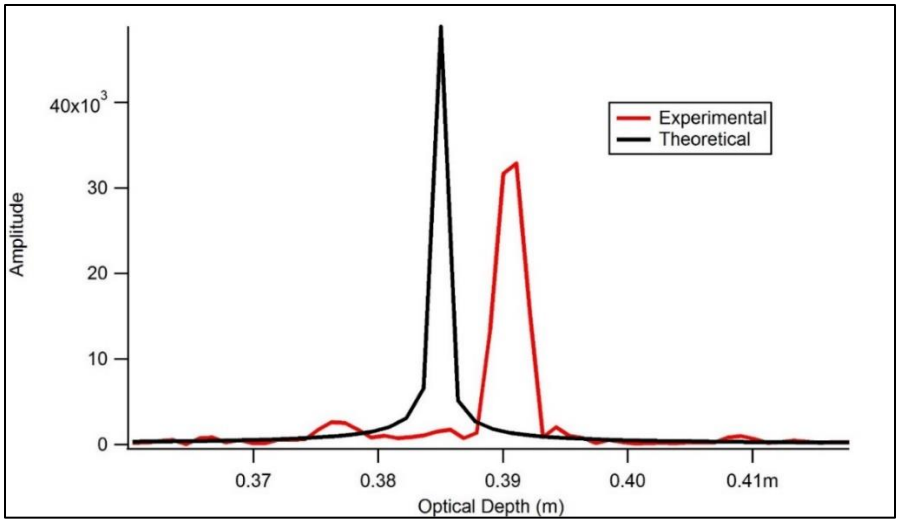

Figure 3.33: Experimental and model FFTs.

Measured distance: $38.5 \pm 0.5\ cm$

Determined from the Theoretical model (FFT peaks): $38.495 \pm 0.004\ cm$

Experimental: $39.060 \pm 0.00424\ cm$

These results overlap with the measured distance range.

3.6 Determining refractive indices of materials

This chapter discusses and presents results of a series of experiments carried out to determine refractive indices of different dielectric materials such as; HDPE, cast Nylon, Delrin. This experiment was an extension of a previous study [14].This work includes a LabVIEW program designed to automate and analyze the data collection leading to calculating refractive index and the author has modified the program to make the data collection more efficient.

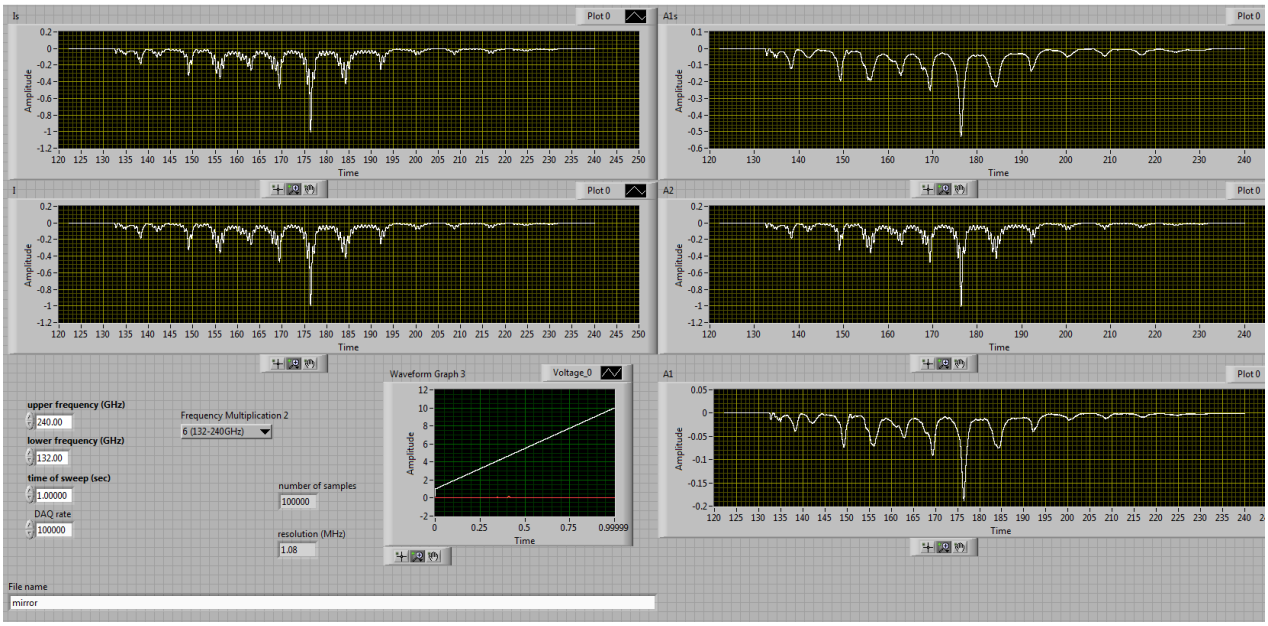

Figure 3.34: Front panel of the Labview program which controls the frequency sweep and their parameters.

For HDPE, two samples with different thicknesses were used.

3.6.1 Procedure:

Apparatus and the setup were almost identical to previous experiments except that mirrors were replaced with rooftop metal plates at 45 degrees to rotate the polarization and the detector was rotated by 90 degrees from its previous orientation. This makes the detector receive only horizontally polarized signals from rooftop metal plates (Figure 3.35). Thus reflections from the surface of the sample and other unwanted reflections are avoided. This reduces the complexity of the interference of beams from near and far

rooftop reflectors. Also, a wire grid polarizer was used in place of the Mylar beam splitter.

The sample of interest was placed in front of the far arm. As the signal passes through the sample, it causes a shift in the frequency due to extra path travelled, when compared to the signal without the sample. This shift is used to determine the index of refraction of the material. To extract the interference term from raw signals, intensity corresponding to each arm was recorded and analyzed.

Thicknesses of samples were measured at different places using a digital micrometer and an average for the thickness was calculated.

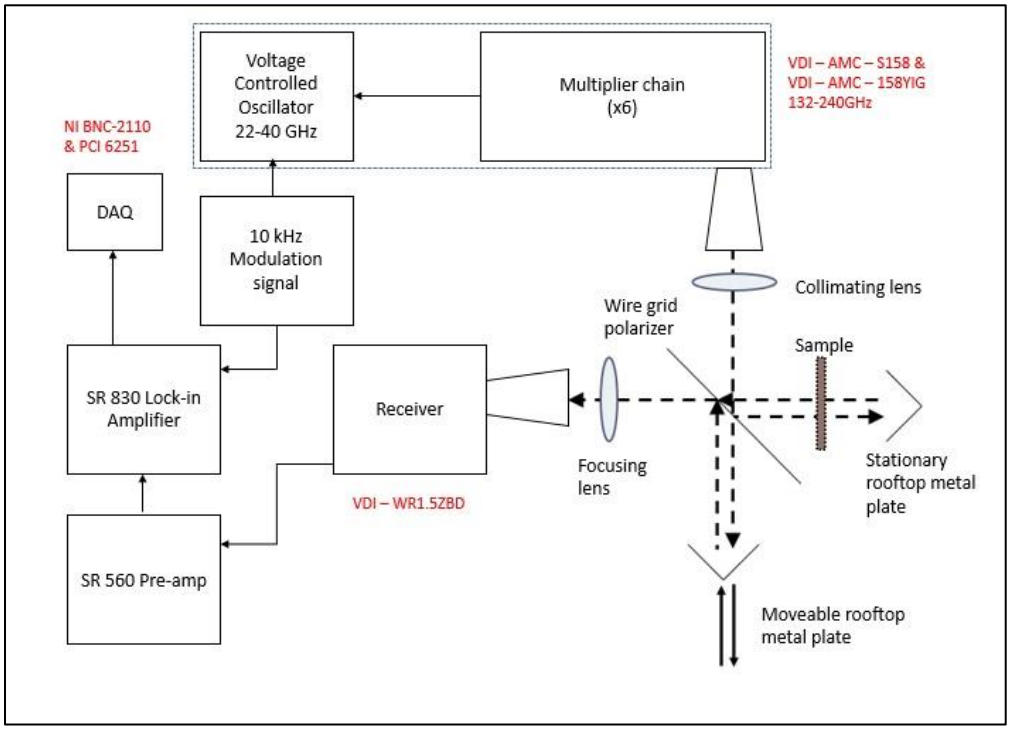

Figure 3.35: Schematic of the setup with a wire grid polarizer and rooftop metal plates.

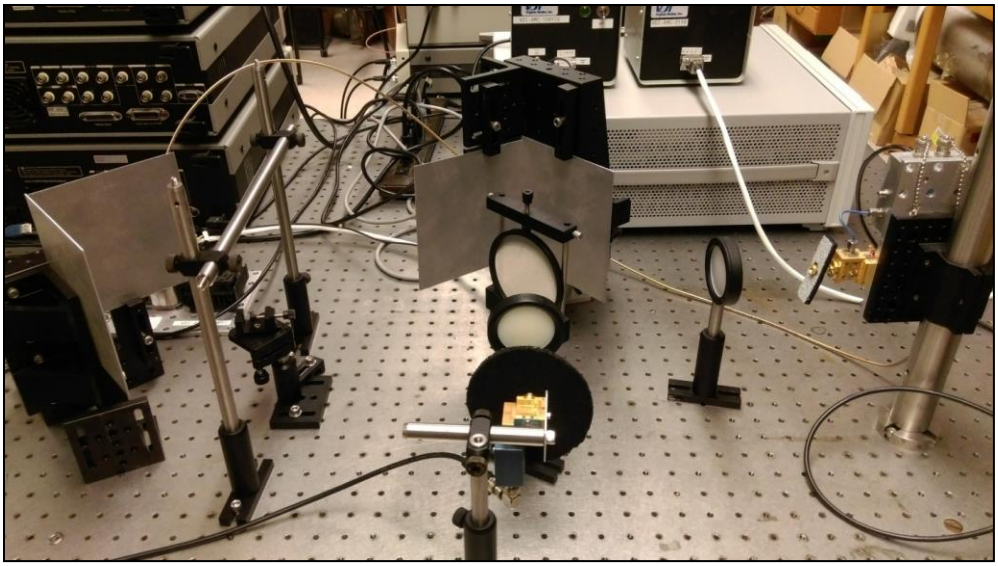

Figure 3.36: Actual setup with roof-top reflectors.

3.6.2 Data analysis

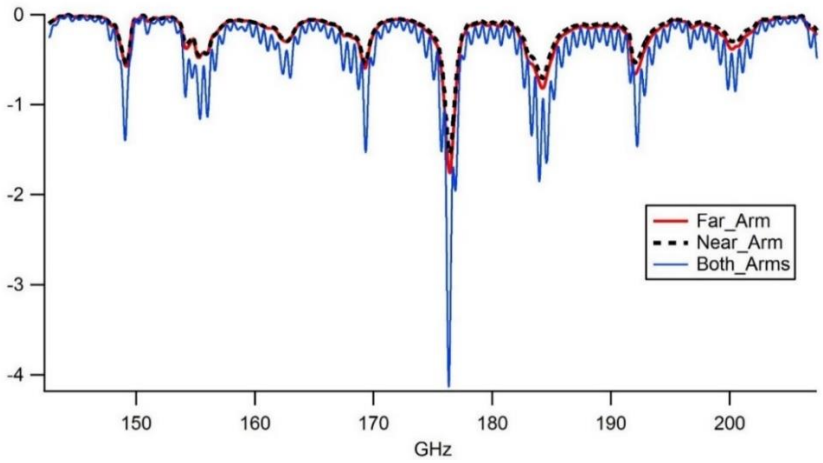

Figure 3.37: Signals from far near and both arms.

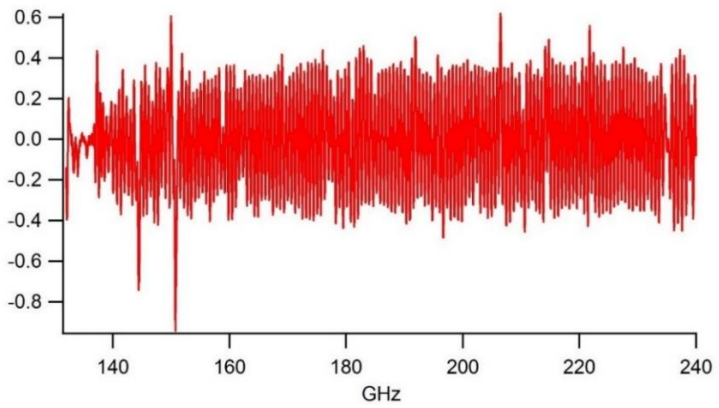

Figure 3.38: Extracted interference pattern after normalization.

Data analysis process was also automated through Igor Pro where a previously written macro was used. The macro includes normalizing and extracting visibility function for the data collected with and without the sample in place, as well as fitting a cosine function for each interference term and to obtain their corresponding FFTs (Figures 3.39 & 3.40). It was observed that the sweep deviated from linearity close to the edges. Therefore, a curve fit was done only to the region where frequency sweep was linear. Finally, it determines the difference in frequency of the fits and requests the user to input sample thickness (Figure 3.41) resulting in refractive index

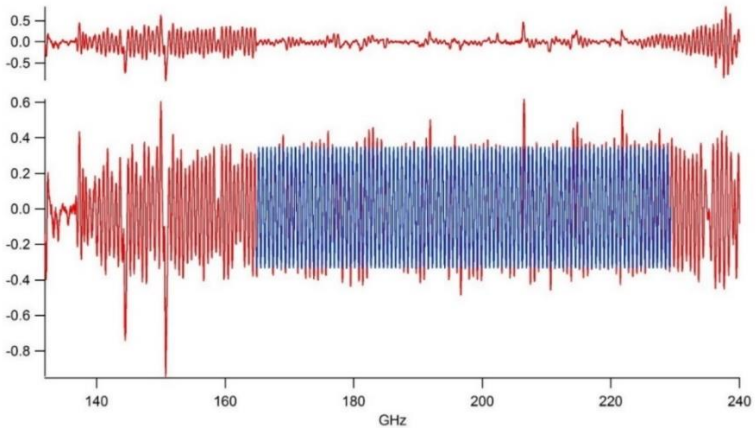

Figure 3.39: Interference pattern without sample, with a fitted cosine function. Top graph is the residual of the fit.

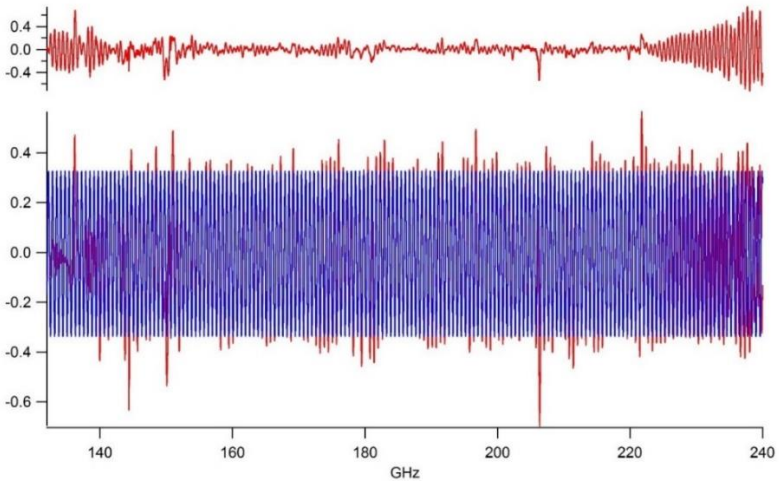

Figure 3.40: Interference pattern with HDPE 6.336 mm sample.

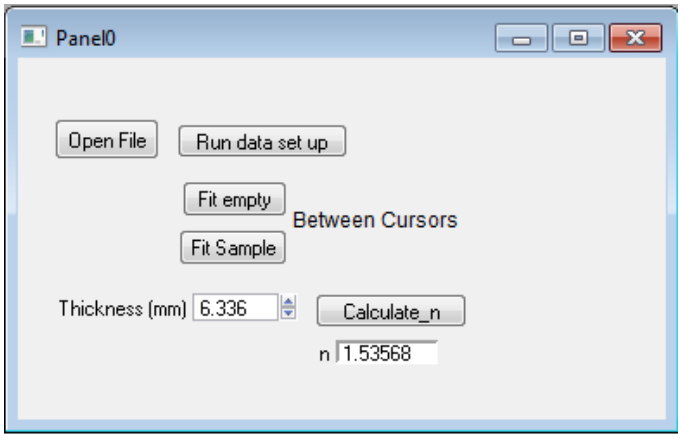

Figure 3.41: Panel for the written macro using Igor –pro.

3.6.3 Refractive Index Results

For each sample, 5 data sets were collected and their average refractive index in presented in the below table alongside its standard deviation.

Sample	Average Thickness (mm)	Average n	Standard deviation
HDPE 1	6.336(1)	1.5355	0.0024
HDPE 2	3.052(1)	1.5355	0.0035
Cast Nylon	19.366(1)	1.7343	0.0015
Delrin	13.5(1)	1.6616	0.0013

Table 3.2: Refractive index results.

Handbook values of HDPE and Cast Nylon are compared with obtained results below [16].

Sample	Handbook value for n	Average of measured n	uncertainty
HDPE	1.523	1.53546	0.00174
Cast Nylon	1.72	1.7342	0.0002

Table 3.3: Handbook and measured refractive indices.

Chapter 4

Conclusions

We have presented a system developed to perform range measurements utilizing FMCW techniques. This system was built around a Michelson Interferometer that was used to record a normalized interferogram. Two separate techniques were used to analyze the data; FFT peaks related to reflections off interfaces were analyzed or fitting functions were used, leading to determining the locations of target interfaces (mirror or dielectric). Frequency was swept with a 108 GHz bandwidth which resulted in a spatial range resolution of ~1.4 mm, consistent with the range resolution, c/2B. We demonstrated that the displacement of a single surface could be monitored to a much higher precision than the range resolution and likely down to ~ 50 μm. However, the FWHM of ~2.7 mm of the FFT of the interferogram will limit the ability to clearly resolve ranges between multiple surfaces to ~3 mm or larger for a bandwidth of ~108 GHz. As shown in the study, these systems did identify reflections from multiple targets along its path, thus enabling experimenters to determine separations between multiple layers.

The experiment was conducted using a homodyne detection system. Main disadvantage with homodyne systems is that they have low sensitivity to diffuse reflections. Therefore,

alignment of the surface normal to the beam's propagation direction is critially. If the system gets misaligned by few degrees, substantial amount of signal would not reach the detector, thus making it difficult to detect the surface. It becomes even more challenging with samples that have uneven surfaces like the clothing sample used in the experiment. On the other hand, heterodyne systems which have a much larger dynamic range should be able to detect diffuse scattering from any surface, relaxing the requirement for the sample to be normal to the incident beam.

The technique described in chapter 3.7 can be considered as an effective method to determine refractive index of an unknown sample; as long as the sample is transparent to THz/sub-millimeter region.

This FMCW system can be further improved to perform velocity measurements of moving targets by detecting the change in phase due to each object's motion within a particular range bin

Further development of this technique will lead to the construction of a physics based 3D imaging system for non-destructive evaluation applications. This can be achieved by combining the system developed in this study, with a FMCW system with phase-sensitive lock-in detection and an optical system to deconvolve multiple surfaces within an FMCW range bin.

References

[1]. J Cooper, K. B., Dengler, R. J., Llombart, N., Talukder, A., Panangadan, A. V., Peay, C. S., Mehdia, I., and Siegel, P. H., “Fast, high-resolution terahertz radar imaging at 25 meters,” Proc. SPIE 7671, (2010). (2013) 34: 152.

[2]. David M. Sheen ; Thomas E. Hall ; Ronald H. Severtsen ; Douglas L. McMakin ; Brian K. Hatchell and Patrick L. J. Valdez, "Standoff concealed weapon detection using a 350-GHz radar imaging system", Proc. SPIE 7670, Passive Millimeter-Wave Imaging Technology XIII, 767008 (2010)

[3]. M. S. Heimbeck and H. O. Everitt, "Off-Axis Fresnel Digital Holography at Terahertz Frequencies," in *Imaging and Applied Optics 2016*, OSA Technical Digest (online) (Optical Society of America, 2016), paper DW2E.2.

[4]. Petkie, D. T., Bryan, E., Benton, C., Phelps, C., Yoakum, J., Rogers, M., & Reed, A. (2008). Remote Respiration and Heart Rate Monitoring with Millimeter-Wave/Terahertz Radars. Proceedings of SPIE, 7117

[5]. Moulton, M. C., Bischoff, M. L., Benton, C., and Petkie, D. T., “Micro-Doppler radar signatures of human activity,” Proc. SPIE, 7837, 78370L (2010).

[6]. Petkie, D. T., Bryan, E., Benton, C., and Rigling, B. D., “Millimeter-wave radar systems for biometric applications,” Proc. SPIE, 7485, 748502 (2009).

[7]. Petkie, D. T., Benton, C., and Bryan, E., "Millimeter wave radar for remote measurement of vital signs." Proc IEEE 2009 Radar Conf., 1-3 (2009).

[8]. Cooper, K. B., Dengler, R. J., Llombart, N., Bryllert, T., Chattopadhyay, G., Schlecht, E., Gill, J., Lee, C., Skalare, A., Mehdi, I., and Siegel, P. H., "Penetrating 3-D imaging at 4- and 25-m range using a submillimeter-wave radar" ,IEEE Transactions on Microwave Theory and Techniques, 56(12), 2771-8 (2008).

[9]. H. Quast, A. Keil, T. Hoyer, and T. Loeffler, "All-electronic 3D terahertz imaging for the NDT of composites," in Proceedings of the 2nd International Symposium on NDT in Aerospace (Singapore Institute of Manufacturing Technology, 2010), paper We.4.B.3.

[10]. Ioachim Pupeza, Rafal Wilk, and Martin Koch, "Highly accurate optical material parameter determination with THz time-domain spectroscopy," Opt. Express 15, 4335-4350 (2007)

[11]. Abbott, B.P., R. Abbott, T.D. Abbott, M.R. Abernathy, F. Acernese, K. Ackley, C. Adams, et al. "GW151226: Observation of Gravitational Waves from a 22-Solar-Mass Binary Black Hole Coalescence." Physical Review Letters 116, no. 24 (June 15, 2016).

[12]. LIGO Detected Gravitational Waves from Black Holes (2016, July 23). Retrieved from https://www.ligo.caltech.edu/detection

[13]. Jesse Zheng, "Optical frequency-modulated continuous-wave interferometers," Appl. Opt. 45, 2723-2730 (2006)

[14]. Zero-Biased Detectors (2016, September 12). Retrieved from http://www.elva-1.com/products/a40039

[15]. Carla Benton ,Optical Characterization of Composites for Quantitative Analysis of Terahertz Images- -Wright State University, Department of Physics

[16]. Polyethylene- High density (HDPE) material information (2016, December 18). Retrieved from http://www.goodfellow.com/E/polyethylene-High-density.html